



ELSEVIER

Contents lists available at ScienceDirect

Progress in Surface Science

journal homepage: www.elsevier.com/locate/progsurf



Review

The thermal near-field: Coherence, spectroscopy, heat-transfer, and optical forces



Andrew C. Jones, Brian T. O'Callahan, Honghua U. Yang,
Markus B. Raschke*

Department of Physics, University of Colorado, Boulder, CO 80309, USA

Department of Chemistry, University of Colorado, Boulder, CO 80309, USA

JILA, University of Colorado, Boulder, CO 80309, USA

ARTICLE INFO

Keywords:

Thermal radiation

Optical near-field

Infrared vibrational spectroscopy

Surface analysis

Thermal transport

ABSTRACT

One of the most universal physical processes shared by all matter at finite temperature is the emission of thermal radiation. The experimental characterization and theoretical description of far-field black-body radiation was a cornerstone in the development of modern physics with the groundbreaking contributions from Gustav Kirchhoff and Max Planck. With its origin in thermally driven fluctuations of the charge carriers, thermal radiation reflects the resonant and non-resonant dielectric properties of media, which is the basis for far-field thermal emission spectroscopy. However, associated with the underlying fluctuating optical source polarization are fundamentally distinct spectral, spatial, resonant, and coherence properties of the evanescent thermal near-field. These properties have been recently predicted theoretically and characterized experimentally for systems with thermally excited molecular, surface plasmon polariton (SPP), and surface phonon polariton (SPhP) resonances.

We review, starting with the early historical developments, the emergence of theoretical models, and the description of the thermal near-field based on the fluctuation–dissipation theory and in terms of the electromagnetic local density of states (EM-LDOS). We discuss the optical and spectroscopic characterization of distance dependence, magnitude, spectral distribution, and coherence of evanescent thermal fields. Scattering scanning near-field microscopy proved instrumental as an enabling technique for the investigations of several of these fundamental thermal near-field properties. We then discuss the role of thermal fields in nano-scale

* Corresponding author.

E-mail address: markus.raschke@colorado.edu (M.B. Raschke).

heat transfer and optical forces, and the correlation to the van der Waals, Casimir, and Casimir–Polder forces. We conclude with an outlook on the possibility of intrinsic and extrinsic resonant manipulation of optical forces, control of nano-scale radiative heat transfer with optical antennas and metamaterials, and the use of thermal infrared near-field spectroscopy (TINS) for broadband chemical nano-spectroscopic imaging, where the thermally driven vibrational optical dipoles provide their own intrinsic light source.

© 2013 Elsevier Ltd. All rights reserved.

Contents

1. Introduction	350
2. Thermal radiation: historical development	351
2.1. Planck's law	354
2.2. Kirchhoff's law – real materials and grey body emission	355
2.3. Far-field thermal emission spectroscopy	356
3. The thermal evanescent near-field	359
3.1. Definition of electromagnetic local density of states (EM-LDOS)	359
3.2. Derivation of the EM-LDOS for a semi-infinite half space	361
3.3. EM-LDOS transition from far- to near-field regime	362
3.4. Spectral distribution of thermal near-fields above representative surface materials	362
3.4.1. Wavevector dependence of EM-LDOS $\rho(z, \omega)$	364
3.4.2. Distance dependence of spectral energy density $u(z, \omega, T)$	366
3.5. Spatial and temporal coherence	366
4. Thermal infrared near-field spectroscopy (TINS)	369
4.1. Measurement of thermal near-field radiation	369
4.2. Scattering-type scanning near-field optical microscopy (s-SNOM)	369
4.3. Thermal infrared near-field spectroscopy: phonon-polariton and molecular resonances	370
4.4. Distance dependence	372
4.5. TINS modeling: tip-sample coupling	373
4.6. TINS as a nano-spectroscopic/nano-imaging technique	376
5. Heat conduction in the thermal near-field	377
5.1. Heat transfer between two parallel planes	378
5.2. Heat transfer between a point-like particle and a planar surface	379
5.3. Heat transfer in non-standard geometries	379
5.4. Nano-scale heat transfer: experiment	379
5.5. Near-field heat transfer: applications	380
6. Thermal near-field optical forces	382
6.1. Vacuum induced forces ($T = 0$ K)	382
6.1.1. Theory of the Casimir force	383
6.1.2. Casimir force: experiment	385
6.2. Thermally induced force (finite temperature)	385
6.2.1. Thermal Casimir force: experiment	387
7. Outlook	388
Acknowledgments	388
References	388

1. Introduction

In this review we will discuss recent advances in the investigation, understanding, and application of the distinct spectral, spatial, and coherence properties of the thermal near-field compared to far-field thermal radiation. In particular, the special resonant enhancement of the near-field electromagnetic

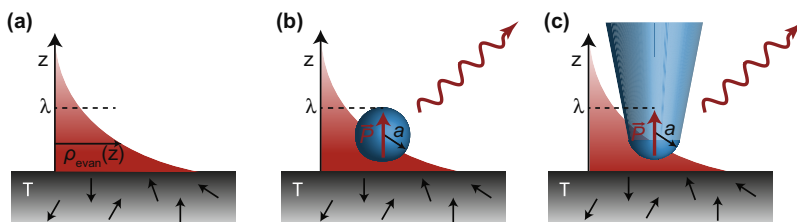


Fig. 1. Surface confined electromagnetic thermal near-field depicted as (a) evanescent electromagnetic local density of states (EM-LDOS) $\rho_{\text{evan}}(z)$ at the interface. The underlying thermally excited fluctuating dipoles and transient currents in the medium (at temperature T) are represented by randomly oriented arrows. (b) A small polarizable sphere in the form of, e.g., a nanoparticle with radius a , can scatter the near-field into detectable far-field radiation (with wavevector up to $|\vec{k}| \sim 1/a$) due to the induced radiating polarization \vec{P} . (c) Similarly, a sharp scanning probe tip with apex radius a , can act as the near-field scatterer. Through the same coupling mechanism, enhanced heat transfer and optical forces are mediated via the evanescent near-field.

local density of states (EM-LDOS) in close proximity to a medium at infrared frequencies opens the door for new forms of surface vibrational spectroscopy and imaging techniques. Thermal infrared near-field spectroscopy (TINS) thus allows for the extension of Fourier transform infrared (FTIR) spectroscopy and microscopy to the nano-scale. Furthermore, we discuss the resonant enhancement of thermal heat transfer on the nano-scale, and the possibility for the resonant control of the Casimir and van der Waals forces.

While far-field thermal emission is well understood, significant recent interest has been devoted to the corresponding properties of evanescent thermal near-fields. This interest has been motivated in part by the emergence of new forms of near-field spectroscopy suitable for the investigation of thermal near-fields and their role in nano-scale heat transfer and optical forces. The relevant length scales for these phenomena are smaller than the characteristic wavelengths of thermal radiation which necessitates a theoretical description which extends beyond far-field thermal radiation and includes the effects of non-propagating near-field modes. The ability to fully harness these effects requires the detailed understanding of thermal near-fields on micro- and nanoscopic length scales. This has been enabled by the development of new scanning near-field microscopy and spectroscopy techniques that provide direct experimental access to the purely evanescent modes for their spectral and spatial characterization (see Fig. 1).

Few reviews and books have yet addressed the fundamental electromagnetic thermal near-field properties [1–3]. In this review, we provide a comprehensive summary of the historical developments, theoretical advances, and recent experimental progress. We perform model calculations to illustrate the vibrationally resonant spectral characteristics for both single-particle molecular vibrational excitations as well as collective phonon-polariton quasiparticle modes. We then discuss experimental results on probing the spectral, spatial, and coherence properties of the associated enhanced EM-LDOS. We include new results from our recent work which demonstrate the capabilities for new forms of surface vibrational spectroscopy and surface chemical analysis with simultaneous nanometer spatial resolution.

The recent advancement in micro- and nano-scale fabrication and experimental techniques has enabled the precise control of separation distances between two structures well below the characteristic wavelength of thermal emission. We discuss the contribution of near-fields to heat transfer in these systems, which can in many cases be the dominant heat transfer mechanism [4,5].

The properties of thermal near-fields determine also other important near-surface phenomena including the van der Waals and Casimir forces that originate from the zero-point fluctuations or as induced by thermal fluctuations. We cover the historic development starting with the work of Lifshitz, the off-resonance interactions at a dielectric surface [6–8], and provide an outlook into the possibility of the resonant optical control of near-field optical forces.

2. Thermal radiation: historical development

The study of thermal radiation has a long and rich history, beginning with the discovery of light invisible to the naked eye within the solar spectrum by William Hershel [9]. Subsequent contributions

by Gustav Kirchhoff in the late 19th century [10] and Max Planck in the early 20th century [11] established the foundations of our understanding of thermal radiation.

The roots of the study of thermal radiation date back over two hundred years. In 1800, William Herschel discovered the infrared contributions to sunlight by placing a thermometer beyond the visible red edge of the solar spectrum as dispersed by a prism, and observed a rise in temperature [9,12]. The discovery of infrared light was followed by the discovery of absorption lines in the solar spectrum by Joseph Fraunhofer in 1814 [13]. In the mid 19th century, Gustav Kirchhoff and Robert Bunsen realized that these absorption lines matched the emission lines of gases heated to incandescence, or of burning materials [10]. A complementary effect was observed when corresponding absorption lines appeared when a broad spectrum of light was transmitted through those gases, an effect Kirchhoff noted as being similar to Fraunhofer's solar observations [12]. This observation led to the development of Kirchhoff's law which states that *for a given material at thermal equilibrium with its surrounding environment, the absorptivity of said material is equal to its emissivity*. Kirchhoff derived this law in Ref. [14], where he applied ray-optics to a radiating hot body in a cavity.

The connection between the absorption of an object and its thermal emission further led Kirchhoff to coin the term “blackbody”, defined as an object that perfectly absorbs incident light at all wavelengths. Following the creation of the concept of a blackbody emitter, the description and experimental characterization of the associated spectral distribution posed a significant challenge for physicists in the late 1800s [15]. Early attempts to describe blackbody emission theoretically were made by Josef Stefan and Ludwig Boltzmann in the mid-19th century. In 1879, Stefan proposed that the total irradiance I emitted from a blackbody is proportional to the fourth power of the temperature T of the object [16],

$$I(T) = \sigma T^4, \quad (1)$$

a result based on a modification of the Dulong and Petit law (see Ref. [17]). Stefan used existing measurements of, e.g., temperature dependent irradiance from a platinum filament by Tyndall [18] to empirically determine the proportionality constant σ . Soon, Boltzmann arrived at the same conclusion using thermodynamic principles, however, an exact form for σ eluded his derivation [19]. Though accurately capturing the temperature dependence of the total irradiance, Eq. (1), known as the *Stefan–Boltzmann law*, provided no information of the *spectral* distribution of the emission.

In the following years, little development of the theoretical model for blackbody emission took place due to the limited experimental data available characterizing the spectral emission. However, advances in lens and grating fabrication had turned spectroscopy into a powerful and precise tool [10,13] and accurate spectral measurements of the thermal emission became possible. At that point, the measurement of blackbody emission was limited by the quality of the emitter. A major advance in the experimental realization of a blackbody was to implement a cavity structure with one small aperture in an otherwise complete closed shell. Light that enters through the aperture would have to bounce many times off the cavity walls before it would re-emerge from the hole. If the walls are sufficiently absorbing, the probability for re-emission through the aperture would be close to zero, resulting in a high absorptivity.

The idea of using a cavity turned out to not only be a clever experimental method for creating a nearly perfect blackbody, but its concept also paved the way for the theoretical descriptions of its emission characteristics. Major advances in the development and measurement of simulated blackbody emission were accomplished by Otto Lummer, Ernst Pringsheim, and Ferdinand Kurlbaum in the late 19th century. They built a cavity as shown in Fig. 2b with heated walls and a small aperture emitting near-perfect blackbody radiation. With this new apparatus, they performed a series of blackbody emission measurements [20,22–25] as shown in Fig. 2c.

Working closely with Lummer and Pringsheim, Wilhelm Wien made pursuits to lay a theoretical framework to describe thermal emission. Notably, using the second law of thermodynamics, Wien developed in 1893 what is now known as *Wien's displacement law*. This law states that the peak emission wavelength of a blackbody is inversely proportional to its temperature [26]. Soon after the first measurements by Lummer et al., Wien also proposed a model (known as *Wien's law*) for the spectral distribution of thermal radiation $\zeta_{\text{bb}}(\nu, T)$ at frequency ν and temperature T

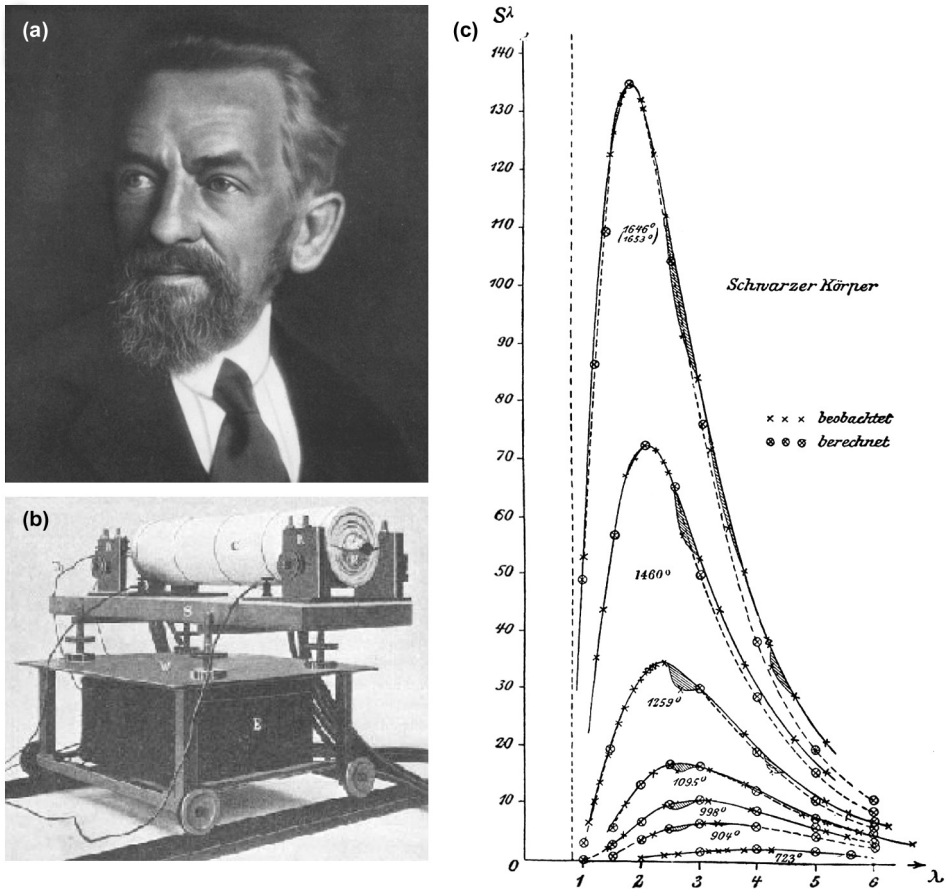


Fig. 2. (a) Photo of Otto Lummer, early pioneer in the measurement of thermal radiation. (b) Cavity used by Lummer, Pringsheim, and Kurlbaum in the 1890's which simulated blackbody radiation. It consisted of a tube of blackened platinum mounted inside a closed ceramic tube with electrically heated walls and one small aperture in its side. (c) Measured spectra of the emission by Lummer and Pringsheim from November 1899. The emitted wavelengths, measured in microns, peak in the infrared for temperatures in the range of 723 to 1646 °C. The crosses are the measured values (beobachtet) and the circled crosses (berechnet) are calculated distributions using Wien's law (Eq. (2)). Figure taken from Refs. [20,21].

$$\zeta_{bb}(v, T) = Av^3 \exp\left(-\frac{Bv}{T}\right), \tag{2}$$

based upon the *ad hoc* notion that thermal radiation is related to molecules with velocities following a Maxwell distribution [27]. The constants A and B in the above expression were yet undetermined but could be obtained from fits to experimental data. Wien's law did fit the short wavelength range quite well. However, the model deviates from the experimental results from Lummer and Pringsheim for long wavelengths.

In early 1900, John William Strutt (Lord Rayleigh) used the idea of equipartition of electromagnetic modes in a cavity to derive an expression for $\zeta_{bb}(v, T)$ given by

$$\zeta_{bb}(v, T) = \frac{8\pi k_B T v^2}{c^3}, \tag{3}$$

where k_B is the Boltzmann constant and c is the speed of light. This expression was later derived more rigorously by James Jeans and is now called the *Rayleigh–Jeans law* [28]. Since the model was based on

the classical notion that all the modes are populated with equal probability, this expression predicted a diverging energy contribution at high frequencies. Known as the ultraviolet catastrophe, this singularity and its correction is discussed further in Section 2.1. Though the Rayleigh–Jeans law matched experimental data in the long wavelength spectral range, the short wavelength spectral range was not well modeled.

In the fall of 1900, Max Planck empirically put forth a function, now called *Planck's law of black-body radiation*, which correctly described the spectral distribution of a blackbody radiator over the entire spectral range

$$\zeta_{\text{bb}}(\nu, T) = \frac{8\pi\nu^2}{c^3} \frac{h\nu}{\exp\left(\frac{h\nu}{k_B T}\right) - 1}. \quad (4)$$

With the empirical factor $h = 6.63 \cdot 10^{-34} \text{ m}^2\text{kg/s}$ (later termed Planck's constant). It was only later that Planck recognized that the average energy of one electromagnetic mode in a cavity should be $k_B T$ if the equipartition theorem is correct, and that his formula would result in Rayleigh–Jeans law if $E(\nu) = h\nu$ shrinks to zero. Using the cavity-mode method pioneered by Rayleigh, Planck developed a more rigorous derivation of the black-body radiation formula in 1906, although was still reluctant to accept the finite “energy elements” $E(\nu) = h\nu$ concept [29].

2.1. Planck's law

We now present a modern quantum optics version of the derivation of the Planck distribution. Consider an enclosure at uniform temperature T . Inside the enclosure, the electromagnetic field can be described by an ensemble of photons¹ forming standing waves with frequency ω and energy E given by $E(\omega) = \hbar\omega$. The spectral mode density $D(\omega)$ or free space density of states (DOS) of photon states in the enclosure is given by

$$D(\omega) = \frac{\omega^2}{\pi^2 c^3}, \quad (5)$$

which is derived by counting the number of states in spherical shells in k -space.

As photons obey Bose–Einstein statistics, in thermal equilibrium the mode occupation number of the photon energy states is given by²

$$n(\omega, T) = \frac{1}{\exp\left(\frac{\hbar\omega}{k_B T}\right) - 1}. \quad (6)$$

The spectral energy density $u_{\text{ff}}(\omega, T)$ may then be expressed as the product of the mode energy $E(\omega)$, mode occupation $n(\omega, T)$, and mode density $D(\omega)$:

$$u_{\text{ff}}(\omega, T) = E(\omega) \cdot n(\omega, T) \cdot D(\omega) \quad (7)$$

$$= \hbar\omega \cdot \frac{1}{\exp\left(\frac{\hbar\omega}{k_B T}\right) - 1} \cdot \frac{\omega^2}{\pi^2 c^3} = \Theta(\omega, T) \cdot D(\omega), \quad (8)$$

where $\Theta(\omega, T) = \hbar\omega / \left(\exp\left(\frac{\hbar\omega}{k_B T}\right) - 1\right)$ is the mean thermal photon energy at frequency ω .

Considering an area element within a volume V , the radiant energy flux through that area element is related to the energy density and the speed of light as $q_{\text{rad}} = u_{\text{ff}}c/4$ [1]. By definition, if a blackbody is placed into that volume, it will absorb all of the incident radiant energy. To remain at thermal equilibrium, it must also emit that same amount of energy. As a result the spectral emissive power of a blackbody ζ_{bb} is given by

¹ Though the quantization of electromagnetic waves had been introduced earlier, the term *photon* was coined in 1923 by Arthur Compton [12].

² It is this contribution from modern quantum mechanics that eliminated the unphysical singularity in the energy density at high frequencies (known as the ultraviolet catastrophe) that puzzled physicists attempting to theoretically describe black-body emission in the late 19th century.

$$\zeta_{\text{bb}}(\omega, T) = \frac{\omega^2}{4\pi^2 c^2} \frac{\hbar\omega}{\exp\left(\frac{\hbar\omega}{k_B T}\right) - 1}. \quad (9)$$

Further, this distribution allows for the exact determination of the Stefan–Boltzmann constant σ in Eq. (1), by integration of the spectral distribution over all frequencies:

$$\sigma = \frac{\pi^2 k_B^4}{60\hbar^3 c^2}. \quad (10)$$

The above derivation is implicitly based on geometric optics.

2.2. Kirchhoff's law – real materials and grey body emission

No ideal blackbody exists, since real materials exhibit electron and lattice vibrational resonances³ and have resulting spectral absorption or emission features. The spectral distribution of the emissive power of a material can be characterized by three parameters: reflection, transmission, and absorption coefficients. Real bodies correspondingly fall between the ideal limits of a perfectly absorbing blackbody, a perfectly reflecting metal, and a perfectly transmissive vacuum as illustrated in Fig. 3a.

Unlike the broad featureless spectrum which constitutes blackbody thermal emission, the resulting thermal emission from real bodies exhibits resonant spectral features associated with the material's properties. Working under the assumption that a body is at uniform temperature at thermal equilibrium and that the fields within the body are not strong enough to modify the intrinsic optical properties by non-linear interactions, Kirchhoff's law states that *the directional-spectral emissivity of the object is equal to its directional spectral absorptivity*.

The directional absorptivity is defined as $\mathcal{A}_\theta(\omega, \theta) = 1 - \mathcal{R}_\theta(\omega, \theta) - \mathcal{T}_\theta(\omega, \theta)$ with $\mathcal{R}_\theta(\omega, \theta)$ and $\mathcal{T}_\theta(\omega, \theta)$ representing the directional reflectivity and transmissivity, respectively, averaged over both s and p polarizations.

Typically, the directional emissivity $\varepsilon_\theta(\omega, \theta)$ is expressed as $\varepsilon_\theta(\omega, \theta) = \mathcal{A}_\theta(\omega, \theta) = 1 - \mathcal{R}_\theta(\omega, \theta)$ under the assumption that an object is either semi-infinite or opaque ($\mathcal{T}_\theta(\omega, \theta) \simeq 0$).⁴ This assumption requires that the characteristic size of the object l is much larger than the penetration depth of radiation δ ($l \gg \delta$). If the directionality is unimportant, the directional quantities may be integrated over θ to get the emissivity, reflectivity, and transmissivity, given by ε , \mathcal{R} , and \mathcal{T} , respectively. Fig. 3a visualizes the interplay of ε , \mathcal{R} , and \mathcal{T} as they vary in relation to one another for a 1 mm slab of different materials at a set of selected wavelengths. For a given material, object size, and emission wavelength, the optical properties fall somewhere in between the ideal limits of a perfect blackbody emitter ($\varepsilon = 1$), a perfect conductor ($\mathcal{R} = 1$), and vacuum ($\mathcal{T} = 1$).

The spectral emissivity $\varepsilon(\omega, T)$ of a given medium is defined as the ratio of the spectral emissive power $\xi_m(\omega, T)$ to that of a blackbody radiator,

$$\varepsilon(\omega, T) = \frac{\xi_m(\omega, T)}{\xi_{\text{bb}}(\omega, T)}. \quad (11)$$

As an example, Fig. 3b and c shows the calculated spectral energy density u_{ff} and emissivity ε for a semi-infinite SiC flat surface at $T = 500$ K. The spectral energy density resembles that of a blackbody over a wide spectral range except in the $\sim 800\text{--}1000$ cm^{-1} band. The deviation from the blackbody emissivity in this spectral range is due to the high reflectivity Reststrahlen band associated with the longitudinal (LO) and transverse (TO) optical phonon resonances in SiC (for details see Section 3.4).

³ Resonances may be either intrinsic single or quasiparticle excitation or extrinsic excitation such as polariton, antenna, or Mie resonances.

⁴ In accordance with the traditional literature, we use the symbol ε to describe the emissivity, not to be confused with the similar symbol ϵ used to describe the dielectric function.

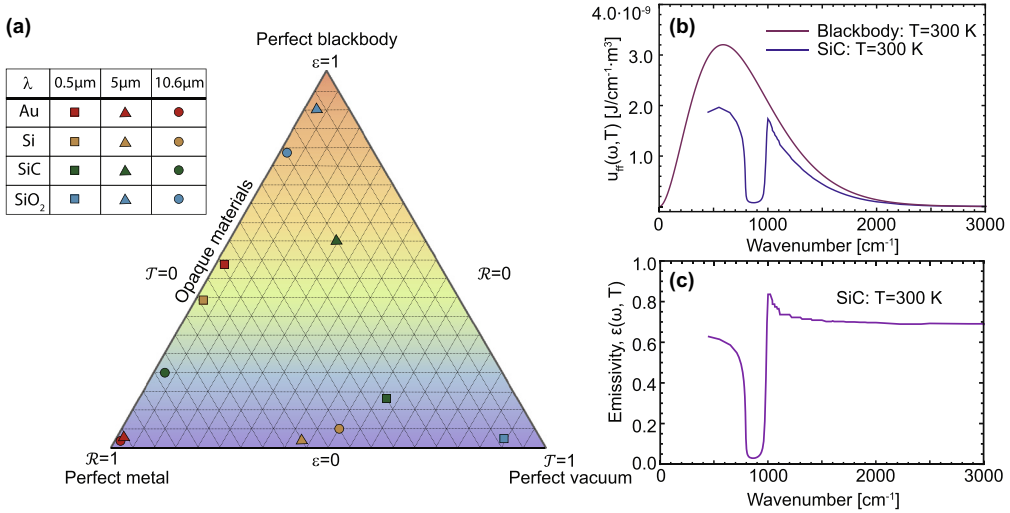


Fig. 3. (a) Emissivity $\varepsilon(\omega)$ of a 1 mm thick slab for several materials (Au, Si, SiC, and SiO₂) at wavelengths of 0.5, 5, and 10.6 μm . This panel illustrates that real materials characteristically deviate from perfect blackbody emissivity through finite reflectivity, transmissivity, and absorptivity. The corners of the triangle represents the ideal limits of a perfect metal, a perfect vacuum, and a perfect blackbody. (b) The difference between the spectral energy density associated with the thermal emission from an ideal blackbody and a real material (SiC as an example). As determined by Kirchhoff's law, the thermal emission of SiC outside its phonon (and electronic) resonant regime is very similar to an ideal blackbody. Strong deviations from a blackbody emission (c) occur between 800 cm^{-1} and 1000 cm^{-1} where SiC is highly reflective due to its Reststrahlen band.

2.3. Far-field thermal emission spectroscopy

The measurement of the spectral emissivity ε of a medium can provide direct spectroscopic information about the spectral dielectric function $\epsilon(\omega)$ and thus the underlying vibrational or electronic properties. The spectroscopic characterization of ε provides the same information as measurements of \mathcal{R} , \mathcal{T} , or \mathcal{A} , since these properties are interrelated as discussed above. However, typical measurements of \mathcal{R} , \mathcal{T} , and \mathcal{A} require the use of an external light source to be directed onto the medium. In contrast, the spectroscopic characterization of the spectral emissivity takes advantage of the medium serving as its own radiative source at finite temperature. This spectroscopic approach is particularly advantageous for systems where external illumination is difficult or even impossible, or where radiation sources covering the spectral range of interest are not readily available. Traditional applications of thermal emission spectroscopy cover a large range from remote surface temperature measurements, study of planetary atmosphere and geology, conducted in the visible/infrared spectral range, and further ranging into THz and radio-frequency applications in astronomy and cosmology, such as the cosmic microwave background detection.⁵

Of particular interest for materials and surface spectroscopy is the infrared vibrational response. Here, the primary challenge in laboratory applications is the discrimination of the sample signal of interest from the broadband room temperature ambient background infrared radiation with its peak emissivity near $\sim 10 \mu\text{m}$. Common approaches to filter the relevant emissivity signal from the background rely on reducing the temperature of the sample environment and implementing modulation techniques. Fig. 4 shows a particularly noteworthy example of thermal emission spectroscopy for surface vibrational spectroscopy [31]. The sample is prepared in an ultrahigh vacuum chamber and

⁵ The cosmic microwave background results from the sudden release of photons during the electron–proton recombination at $\sim 3.8 \times 10^5$ years after the Big Bang. At that time, the temperature of the universe was $\sim 4 \times 10^3$ K, emitting thermal blackbody radiation peaked in the near-infrared. With the 10^7 volumetric expansion of the universe to its present size, that radiation redshifted to the microwave frequency range [30].

held at a temperature of 310 K. The thermal radiation emitted from the sample is collected with IR optics with baffles and radiation shields cooled to liquid nitrogen temperature. The spectrometer itself is liquid He cooled to 5 K, and emission is measured at grazing angle of emission to maximize sensitivity with respect to surface-normal adsorbate vibrational modes. The high sensitivity and contrast of this approach allowed for the vibrational spectroscopic characterization of CO adsorption on Ni(100) with monolayer [32] and even sub-monolayers [31] sensitivity as shown in Fig. 4b. The growth in surface coverage with increasing exposure from 0.2 to 0.5 Langmuir is seen from the evolution of the characteristic on-top ($\sim 2030\text{ cm}^{-1}$) and bridge site ($\sim 1900\text{ cm}^{-1}$) C=O stretch resonances. The concomitant observation of the weak molecule-substrate Ni-CO mode at $\sim 475\text{ cm}^{-1}$ provided insight into the structural disorder. It is noteworthy to point out the peaked thermal emission associated with the

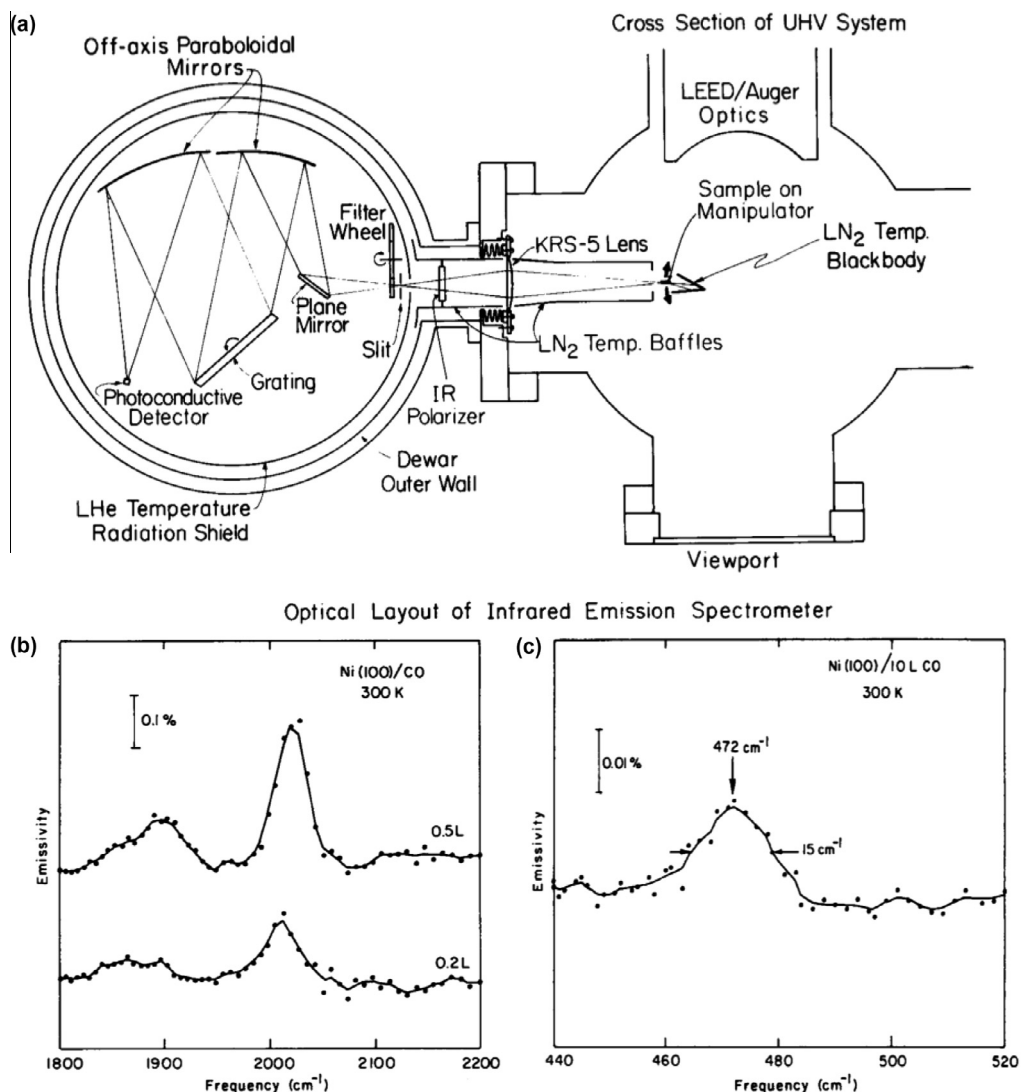


Fig. 4. (a) Far-field thermal infrared emission spectroscopy with ultrahigh vacuum sample chamber and liquid He cooled spectrometer. The extreme sensitivity of this apparatus allows for the characterization of the emissivity of molecular adsorbates on single crystal metal surfaces. Thermal emission spectra are obtained for the C=O (b) and Ni-CO (c) stretch modes of CO on Ni(100) with sub-monolayer sensitivity. Figure taken from Ref. [31].

vibrational resonances of the molecular monolayer. This behavior differs from the emission as would be seen from a semi-infinite geometry of the same material where characteristic dips in the emissivity would be observed in conjunction with spectral regions that exhibit elevated reflectivity.

The differences between these two scenarios can be explained via Kirchhoff's law, which again states that the absorptivity of an object is equal to its emissivity. For example, a single molecule will exhibit peaked thermal emission as it is only able to emit thermal radiation at frequencies at which it has absorptive modes. Similarly, for a thin layer of material, with thickness t less than the absorption/skin-depth $\delta(\omega)$, the layer primarily absorbs light in the spectral regions where the absorption coefficient for the material is peaked. The thermal emission is correspondingly peaked in the spectral regions associated with these resonant absorption features. This experimental scenario applies to the experiment discussed above and shown in Fig. 4a. The high reflectivity metal surface results in a broadband low-emissivity background while the molecular layer adsorbed on the surface exhibits characteristic peaks as shown in Fig. 4b and c.

In contrast, for slabs of material of thickness $t > \delta(\omega)$ in the relevant spectral range, light which enters through the upper interface of the slab is absorbed. As the thick slab is broadly absorptive, the spectral distribution of its thermal emission is correspondingly broad. Deviations from the ideal blackbody occur only when light fails to enter the medium because of a finite reflectivity of the medium surface at certain resonance frequencies. The finite reflectivity results in the characteristic dips in emissivity. The limit for this scenario is the case of an opaque or semi-infinite body ($\mathcal{T} = 0$), where the emissivity of the system is defined as $\varepsilon(\omega) = 1 - \mathcal{R}(\omega)$. The corresponding thermal emission spectrum consequently exhibits characteristic dips associated with regions of elevated reflectivity as illustrated in Fig. 5.

Thickness dependent emissivity from a Polytetrafluoroethylene (PTFE) slab, obtained from reflectivity and transmissivity calculations based on spectroscopic ellipsometry data [33], is displayed in Fig. 5. For thicknesses less than the skin depth, the emission peaks at the C–F vibrational frequencies. As the thickness increases, the absorptivity progressively broadens as the increase of material quantity leads to significant non-resonant absorption. For a thick slab, the emissivity is broadband with dips at spectral location where the reflectivity is peaked.

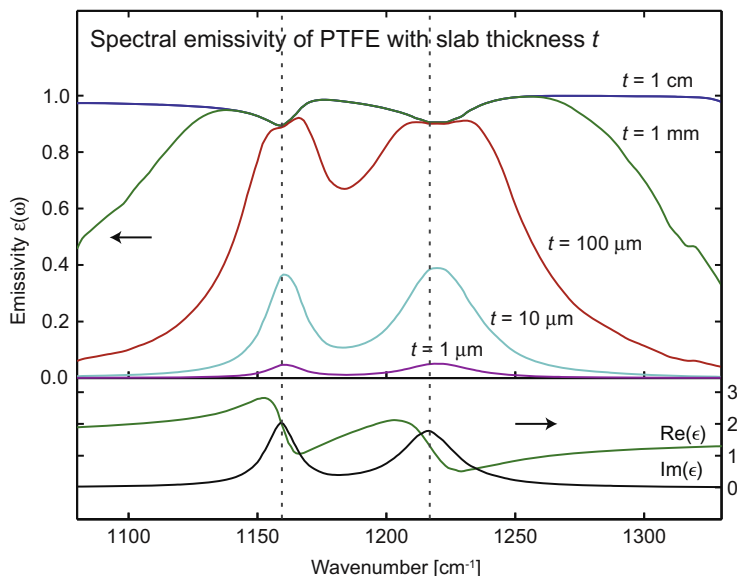


Fig. 5. Calculated thermal emissivity of slabs of PTFE of different thickness t . For thicknesses less than the skin depth (1 and 10 μm) the emissivity peaks at absorption maxima due to the symmetric and anti-symmetric C–F stretch modes. As the thickness increases a broadband emission emerges where the otherwise weak off-resonant absorption contributions become significant. The emission from a thick slab (1 cm) then exhibits dips corresponding to the increased reflectivity on resonance. Calculation based on spectroscopic ellipsometry data for PTFE [33].

3. The thermal evanescent near-field

While the Planck model for a blackbody radiator and its modification for a grey body emission provides an excellent description of far-field thermal radiation, it fails to give insight into the nature of thermal radiation in the near-field regime. For distances above a medium shorter than the wavelength of the emitted radiation, a model which includes near-field effects is required. The energy density near the surface can be much greater than the free space DOS discussed in the previous section. Given its evanescent, i.e., non-propagating character, the near-field is spatially localized and its amplitude is expected to increase rapidly with decreasing distance from the surface of the medium. Thus, when two objects are placed apart at a distance much smaller than the characteristic wavelength of thermal radiation, i.e., in the near-field, evanescent field coupling can occur and cause significant enhancement of the radiative energy transfer between two media.

In order to understand the thermal near-field, a model which incorporates the actual fundamental microscopic source polarization or currents is required. The following section will summarize the theoretical description [2,34–36] of the thermal near-field and how its spatial, spectral, and coherence properties can drastically differ from their far-field counterparts. Fig. 6a shows schematically the microscopic origin of the thermal radiation as thermal fluctuations exciting transient dipoles or currents generating the underlying source polarization in the medium. In order to obtain the spatial near-field distribution one has to sum the fields at any given point in space from all individual sources.

3.1. Definition of electromagnetic local density of states (EM-LDOS)

The electromagnetic local density of states (EM-LDOS) $\rho(\vec{r}, \omega)$ is an extension of the concept of the DOS $D(\omega)$ in order to incorporate the spatial dependence for an inhomogeneous geometry, i.e., a spatial dependence in the vicinity of a medium [36]. To derive an expression for the EM-LDOS in terms of the dielectric function for a given material, we consider a body at temperature T in thermal equilibrium with its environment. Similar to Eq. (8) where the spectral energy density $u_{\text{ff}}(\omega, T)$ is defined in terms of the density of states $D(\omega)$ for positive ω , the local spectral energy density $u(\vec{r}, \omega, T)$ may be written in terms of the EM-LDOS $\rho(\vec{r}, \omega)$ as,

$$u(\vec{r}, \omega, T) = \rho(\vec{r}, \omega) \cdot \frac{\hbar\omega}{\exp\left(\frac{\hbar\omega}{k_B T}\right) - 1} = \rho(\vec{r}, \omega) \cdot \Theta(\omega, T). \tag{12}$$

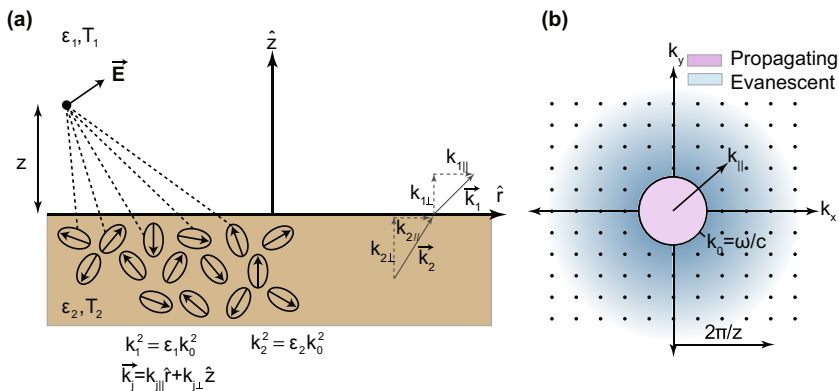


Fig. 6. Schematic of the parameters used in the description of the EM-LDOS associated with a semi-infinite planar half-space. (a) The fluctuational currents or polarization within the medium are related to the induced radiation field through the Green's Dyadic function for the system [37]. The wave-vector components in the parallel and perpendicular directions to the surface plane associated with the field are displayed on the right side of (a). (b) A qualitative depiction of the contribution to the total EM-LDOS from the propagating far-field waves ($k_{||} < k_0$) and evanescent solutions ($k_{||} > k_0$).

$\rho(\vec{r}, \omega)$ is material and geometry dependent. Later, we will find an expression for $\rho(\vec{r}, \omega)$, which yields a tractable integral expression in the special case of a semi-infinite planar half-space geometry. $u(\vec{r}, \omega, T)$ is related to the optical electric and magnetic fields through the fundamental relation,

$$u(\vec{r}, \omega, T) = \frac{\epsilon}{2} \langle |E(\vec{r}, \omega)|^2 \rangle + \frac{\mu}{2} \langle |H(\vec{r}, \omega)|^2 \rangle. \quad (13)$$

Starting with the microscopic picture of a fluctuating current density distribution, two requirements exist in determining $u(\vec{r}, \omega, T)$ outside the medium for a given thermal body: (1) it is necessary to establish the relationship between a thermal current element within the material and the resulting electromagnetic field outside the thermal body, and (2) the statistics of the fluctuating current distribution must be described [2].

To satisfy the first requirement, the electric and magnetic fields outside the material associated with a given electric $\vec{j}(\vec{r})$ or magnetic $\vec{m}(\vec{r})$ current density inside the material may be established using the Green's dyadic functions under consideration of the system geometry:

$$E(\vec{r}, \omega) = i\mu_0\omega \int \vec{G}^E(\vec{r}, \vec{r}_b, \omega) \cdot \vec{j}(\vec{r}_b, \omega) d^3\vec{r}_b, \quad (14)$$

$$H(\vec{r}, \omega) = \int \vec{G}^H(\vec{r}, \vec{r}_b, \omega) \cdot \vec{m}(\vec{r}_b, \omega) d^3\vec{r}_b. \quad (15)$$

Here, the quantities \vec{G}^E and \vec{G}^H are the Green's dyadic functions for the specific system geometry relating the current within the material to the field generated above the interface, and have integral expression given in Ref. [38]. The integral over $d^3\vec{r}_b$ is taken over the volume of the entire thermal body [36].

The second requirement is met via the application of the *fluctuation–dissipation theorem* which relates the power spectrum of the fluctuational current density to the loss mechanisms for those currents in the material. Here, the correlation function of the statistical fluctuations of the current density distribution can be related to the imaginary part of the dielectric permittivity of the medium [2],

$$\langle j_i(\vec{r}, \omega) j_j(\vec{r}', \omega') \rangle = 4\pi\epsilon_0\omega \text{Im}[\epsilon(\omega)] \cdot \Theta(\omega, T) \delta_{ij} \delta(\vec{r} - \vec{r}') \delta(\omega - \omega'). \quad (16)$$

Following the derivation and definition of the EM-LDOS in Ref. [36], we introduce the correlation functions \mathcal{E}_{ij} and \mathcal{H}_{ij} for the electric and magnetic fields, respectively, for a stationary system:

$$\mathcal{E}_{ij}(\vec{r}, \vec{r}', \omega, \omega') = \langle E_i(\vec{r}, \omega) E_j^*(\vec{r}', \omega') \rangle, \text{ and} \quad (17)$$

$$\mathcal{H}_{ij}(\vec{r}, \vec{r}', \omega, \omega') = \langle H_i(\vec{r}, \omega) H_j^*(\vec{r}', \omega') \rangle. \quad (18)$$

These relations quantify the correlation of the fields in space and time (and will be important in the discussion of near-field coherence effects in Section 3.5). Implementing both Green's dyadics (Eq. (15)) and the fluctuation–dissipation theorem (Eq. (16)), the expressions for the correlation functions can be derived [36]:

$$\mathcal{E}_{ij}(\vec{r}, \vec{r}', \omega) = \Theta(\omega, T) \cdot \frac{\mu_0\omega}{2\pi} \text{Im} \left\{ G_{ij}^E(\vec{r}, \vec{r}', \omega) \right\}, \text{ and} \quad (19)$$

$$\mathcal{H}_{ij}(\vec{r}, \vec{r}', \omega) = \Theta(\omega, T) \cdot \frac{\epsilon_0\omega}{2\pi} \text{Im} \left\{ G_{ij}^H(\vec{r}, \vec{r}', \omega) \right\}. \quad (20)$$

Considering only positive frequencies, the spectral energy density $u(\vec{r}, \omega, T)$ can be expressed in terms of the correlation functions and thus the dyadic Green's functions:

$$u(\vec{r}, \omega, T) = 4 \left\{ \left(\frac{\epsilon_0}{2} \right) \sum_{i=1,3} \mathcal{E}_{ii}(\vec{r}, \vec{r}, \omega) + \left(\frac{\mu_0}{2} \right) \sum_{i=1,3} \mathcal{H}_{ii}(\vec{r}, \vec{r}, \omega) \right\} \quad (21)$$

$$= \Theta(\omega, T) \cdot \frac{\omega}{\pi c^2} \text{Im} \left\{ \text{Tr} \left(\vec{G}^E(\vec{r}, \vec{r}, \omega) + \vec{G}^H(\vec{r}, \vec{r}, \omega) \right) \right\}. \quad (22)$$

By comparing this expression with the definition for the EM-LDOS given by Eq. (12), we arrive at an expression for the EM-LDOS $\rho(\vec{r}, \omega)$ in terms of the dyadic Green's function for the system [36],

$$\rho(\vec{r}, \omega) = \frac{\omega}{\pi c^2} \text{Im} \left\{ \text{Tr} \left(\vec{G}^E(\vec{r}, \vec{r}, \omega) + \vec{G}^H(\vec{r}, \vec{r}, \omega) \right) \right\}. \tag{23}$$

This procedure allows one to express the EM-LDOS in terms of the familiar dyadic Green’s functions, which in turn are solutions of the vector electromagnetic Helmholtz equation $\nabla \times \nabla \times \vec{G}^{E,H}(\vec{r}, \vec{r}', \omega) - k^2 \vec{G}^{E,H}(\vec{r}, \vec{r}', \omega) = \vec{I} \delta(\vec{r} - \vec{r}')$. The Green’s functions allow for a simple expression for the EM-LDOS and contain all the details of the specific geometry, boundary conditions, and material properties.

3.2. Derivation of the EM-LDOS for a semi-infinite half space

In the following section we discuss the EM-LDOS function $\rho(\vec{r}, \omega)$ that can be obtained for a semi-infinite half-space above a medium with planar termination, along with the associated spectral energy density $u(\vec{r}, \omega, T)$ [2,36]. The system geometry in this case is defined by a semi-infinite planar half space medium ($z > 0$) of complex dielectric permittivity $\epsilon_1(\omega)$ and a lower semi-infinite planar half space medium ($z \leq 0$) of complex dielectric permittivity $\epsilon_2(\omega)$. The media of both the upper and lower half spaces are assumed to be linear, isotropic, and non-magnetic, and in general have frequency dependent dielectric permittivities.

The Green’s function for that system correlates the microscopic current density element at a given location in the lower half space with the electric field generated, and accounts for their presence in the upper half space by incorporating the Fresnel reflection coefficients of the planar surface separating the two half-spaces [37]. Combination of the Green’s dyadic function with the fluctuation–dissipation theorem then provides the expression of the EM-LDOS $\rho(z, \omega)$, at a given frequency ω , and height above a material z , in terms of an integral over the in-plane wavevector component k_{\parallel} from zero to infinity [2,36,39],

$$\rho(z, \omega) = \frac{\rho_v(\omega)}{2} \left\{ \underbrace{\int_0^{\omega/c} \frac{k_{\parallel}}{k_0 |k_{1,\perp}|} \frac{2 - |r_{12}^s|^2 - |r_{12}^p|^2}{2} dk_{\parallel}}_{\text{propagating}} + \underbrace{\int_{\omega/c}^{\infty} \frac{k_{\parallel}^3}{k_0^3 |k_{1,\perp}|} \{ \text{Im}(r_{12}^s) + \text{Im}(r_{12}^p) \} e^{-2\text{Im}(k_{\perp,1})z} dk_{\parallel}}_{\text{evanescent}} \right\}. \tag{24}$$

The three unit vectors \hat{x} , \hat{y} , and \hat{z} define the spatial position $\vec{r} = x\hat{x} + y\hat{y} + z\hat{z}$ and wavevectors $\vec{k} = k_x\hat{x} + k_y\hat{y} + k_z\hat{z}$. For simplicity, these vectors can be expressed in terms of their in- and out-of-plane contributions as $\vec{r} = \vec{R} + \vec{z}$ and $\vec{k} = \vec{k}_{\parallel} + \vec{k}_{\perp}$, where $\vec{R} = x\hat{x} + y\hat{y}$, $\vec{k}_{\parallel} = k_x\hat{x} + k_y\hat{y}$, $\vec{k}_{\perp,i} = k_z\hat{z}$, and $k_0 = \omega/c$. Fig. 6a) shows the relationship of these wavevectors between both the upper and lower medium. $\rho_v(\omega) = \omega^2/\pi^2 c^3$ is the vacuum density of states (equivalent to the free space density of states $D(\omega)$ in Eq. (5)).

Eq. (24) expresses the EM-LDOS as a function of height z above a planar surface as a sum of evanescent and propagating contributions. Propagating contributions correspond to values of k_{\parallel} smaller than the free-space wavevector k_0 ; evanescent contributions correspond to values of k_{\parallel} which are greater than the free-space wavevector k_0 .

The quantities r_{12}^s and r_{12}^p are the Fresnel reflection coefficients at the boundary between the two media for s and p polarization, expressed in terms of the in- and out-of-plane components of the wavevector,

$$r_{12}^p = \frac{-\epsilon_1 k_{\perp,2} + \epsilon_2 k_{\perp,1}}{\epsilon_1 k_{\perp,2} + \epsilon_2 k_{\perp,1}}, \text{ and} \tag{25}$$

$$r_{12}^s = \frac{k_{\perp,1} - k_{\perp,2}}{k_{\perp,1} + k_{\perp,2}}. \tag{26}$$

Finally k_{\parallel} and $k_{\perp,n}$ in the upper and lower half-spaces ($n = 1,2$) are related to one another by the dispersion relation for light $\epsilon_n \mu_n k_0^2 = k_{\perp,n}^2 + k_{\parallel}^2$ with $\text{Im}(k_{\perp,n}) > 0$ and $k_0 = \omega/c$ [2].

3.3. EM-LDOS transition from far- to near-field regime

Without loss of generality, for the following discussion we consider the medium–vacuum interface with $\epsilon_1 = 1$. In the far-field ($z \gg \lambda$) only in-plane wavevectors, corresponding to propagating solutions in the first term of Eq. (24) may contribute to the EM-LDOS ($k_{\parallel} < k_0, k_{\perp,n} \in \mathbb{R}$). As expected, the far-field spectral energy density associated with Eq. (24) reduces to the classical solution defined by Kirchhoff emissivity $\epsilon(\omega)$ and the Planck distribution $u_{\text{ff}}(\omega, T) = \epsilon(\omega) \cdot u_{\text{bb}}(\omega, T)$ [40]. The second integral in Eq. (24) is negligible due to its exponential decay term, and the first integral just reduces to Kirchhoff's law for an opaque body (i.e., $\epsilon = 1 - \mathcal{R}$). Further, the result for a blackbody may then be obtained by setting the reflection coefficients to zero.

While the far-field contribution to the EM-LDOS is still present for sub-wavelength distances above the surface ($z < \lambda$) the evanescent waves described by the second integral of Eq. (24) ($k_{\parallel} > k_0$ for which $k_{\perp,1} \in \mathbb{Im}$) begin to become significant and at very short distances dominate the EM-LDOS.

In the quasi-static limit ($z \ll \lambda$, or $k_{\parallel} \gg k_0$)⁶ the Fresnel reflection factors reduce to $r_{12}^s = 0$ and $r_{12}^p = (\epsilon_2 - 1)/(\epsilon_2 + 1)$ [2,36]. Using the relation $\text{Im}\{(\epsilon - 1)/(\epsilon + 1)\} = 2\text{Im}(\epsilon)/|\epsilon + 1|^2$, Eq. (24) further simplifies to,

$$\rho_{\text{evan}}(z, \omega) \simeq \frac{1}{\pi^2 \omega} \frac{\text{Im}(\epsilon_2)}{|\epsilon_2 + 1|^2} \int_{\omega/c}^{\infty} k_{\parallel}^2 \exp(-2k_{\parallel}z) dk_{\parallel} = \frac{1}{4\pi^2 \omega z^3} \frac{\text{Im}(\epsilon_2)}{|\epsilon_2 + 1|^2}. \quad (27)$$

This expression illustrates the z^{-3} distance dependence and strong resonant enhancement of the EM-LDOS either through resonance in $\text{Im}(\epsilon_2)$ or via the surface polariton resonance condition $\text{Re}(\epsilon_2) = -1$.

Polaritons are collective quasiparticle excitations between the electromagnetic field and a resonant polarization oscillation in the material. Polaritons are excited by an electromagnetic wave exciting a collective charge or lattice oscillation. If the excitation is at the interface of two different materials, the resulting surface wave is called a *surface polariton* (SP) [41]. SPs may be either standing or propagating, and are surface confined in the sense that the generated electromagnetic fields decay evanescently from the interface. The underlying quasiparticle excitation further classify SPs. For example, surface plasmon polaritons (SPPs) are due to electron plasma excitations while the origin of surface phonon polaritons (SPhPs) are optical phonons. At an air–dielectric interface, SPs satisfy the dispersion relation

$$k_{\parallel} = \frac{\omega}{c} \sqrt{\frac{\epsilon_2}{\epsilon_2 + 1}}, \quad (28)$$

and are resonant at a frequency when

$$\text{Re}(\epsilon_2) = -1. \quad (29)$$

3.4. Spectral distribution of thermal near-fields above representative surface materials

In order to illustrate the spatial and spectral behavior of $u(z, \omega, T)$ and $\rho(z, \omega)$ we consider three representative materials with characteristic vibrational modes: polytetrafluoroethylene (PTFE), quartz (SiO_2), and silicon carbide (SiC). SiO_2 and SiC support phonon-polariton excitations, and their measured dielectric functions at optical frequencies are plotted in Fig. 7. PTFE is an example of a material with local molecular vibrational resonances with characteristic symmetric and anti-symmetric C–F infrared-active vibrational stretch modes. We use the theory discussed above to calculate the spatial and spectral behavior of $\rho(z, \omega)$ and $u(z, \omega, T) = \Theta(\omega, T) \cdot \rho(z, \omega)$ for these three materials.

Using the dielectric functions $\epsilon(\omega)$ measured from spectroscopic ellipsometry for each of these materials, the EM-LDOS $\rho(z, \omega)$ and the associated spectral energy density $u(z, \omega, T)$ can be calculated fully numerically for specific heights above the surface using Eq. (24). Fig. 8 shows the changes in magnitude and spectral distribution of $u(z, \omega, T)$ for $z = 100, 10, 1, \text{ and } 0.1 \mu\text{m}$ indicating the transition from

⁶ Quasi-static limit: retardation and associated phase effects are neglected which is typically valid for distances or dimensions $< \lambda/20$ to a good approximation.

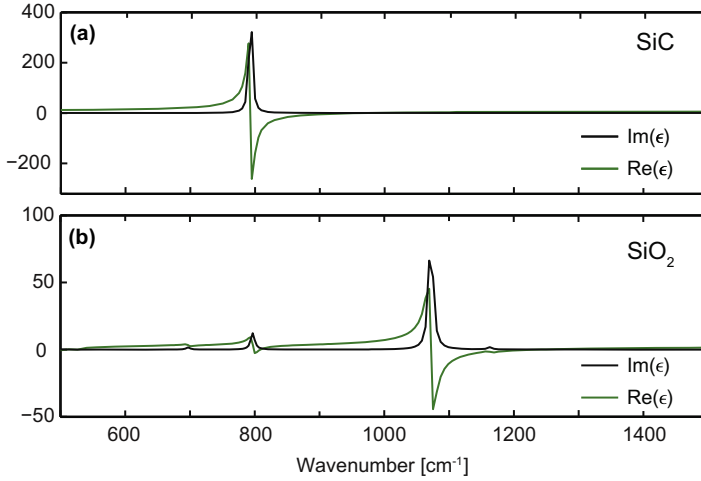


Fig. 7. Dielectric functions of SiC (a) and SiO₂ (b) showing the influence of bulk TO phonon modes at 797 cm⁻¹ and 1070 cm⁻¹, respectively [42].

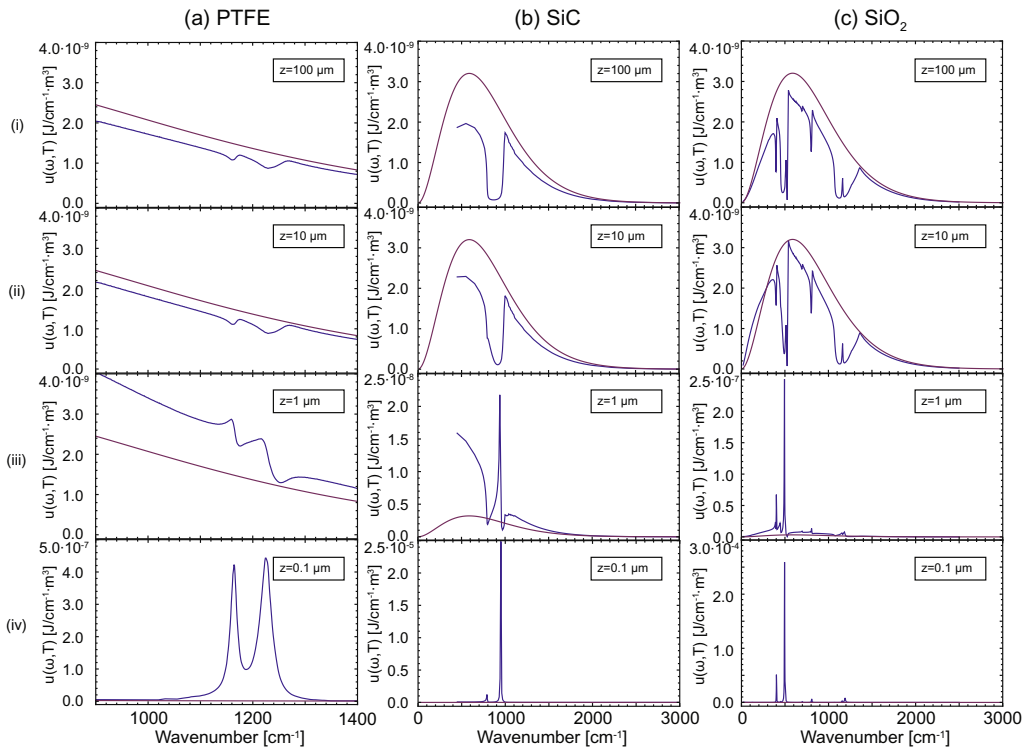


Fig. 8. The calculated spectral energy density $u(z, \omega, T)$ (blue-lines) for PTFE (a), SiC (b), and SiO₂(c) surfaces at representative distances of $z = 100, 10, 1,$ and $0.1 \mu\text{m}$ (i–iv, respectively) indicative of the transition from the radiative far-field regime (i, ii) to the near-field regime (iii, iv). Peaks in $u(z, \omega, T)$ at short distances represent molecular resonances (a, PTFE) or the SPHP excitation conditions (b, SiC and c, SiO₂). The spectral energy density of an ideal blackbody radiator is shown for reference (purple lines). Temperature $T = 300 \text{ K}$. (For interpretation of the references to color in this figure legend, the reader is referred to the web version of this article.)

the far-field to the near-field. In the far-field (i, ii), the calculations of the spectral energy density $u(z, \omega, T)$, as expected from Kirchhoff's law, show a decrease in $u(z, \omega, T)$ on SPhP resonance compared to a blackbody. For PTFE (a), the deviation is due to the C–F molecular resonances at 1158, 1210, and 1240 cm^{-1} (latter two not spectrally resolved) [43,44]. While for SiC and SiO₂, the deviations occur where the materials exhibit heightened reflectivity in the Reststrahlen band associated with the SPhP of the longitudinal optical (LO) and transverse optical (TO) phonon modes of the material, for SiC at 797 and 971 cm^{-1} respectively, and for SiO₂ in the range of 1050–1250 cm^{-1} [45,46]. As the near-field contributions become significant for distances $z \lesssim \lambda$ (iii), $u(z, \omega, T)$ starts to exceed the far-field blackbody spectrum, over the entire spectral range, but most prominently on resonance.

In the near-field regime (iv), the peaks in the spectral energy density $u(z, \omega, T) = \Theta(\omega, T) \cdot \rho(z, \omega)$ for each material can also be described with the approximate quasi-static form of $\rho(z, \omega)$ (Eq. (27)). For PTFE, peaks occur at the maxima in the imaginary part of the permittivity $\text{Im}(\epsilon_{\text{PTFE}})$ at the vibrational molecular resonances. For SiC and SiO₂, both the peaks represent the resonance conditions for SPhP excitation given by Eq. (29).

The calculations shown in Fig. 8 demonstrate that these surface wave resonances result in a drastic enhancement in $u(z, \omega, T)$, for example by a factor of 700 increase for PTFE at $\omega = 1158 \text{ cm}^{-1}$ at $z = 100 \text{ nm}$ compared to the far-field $u(\omega, T)$. For SiC the SPhP resonance condition (Eq. (29)) is met at a frequency of $\omega_{\text{SPhP}} = 950 \text{ cm}^{-1}$ in between the LO and TO phonon frequencies. For SiO₂, due to the presence of multiple phonon modes, the SPhP resonance condition is met at several spectral positions. The relative strengths of these SPhP resonances are given by the value of the imaginary component of the dielectric function at that frequency, which represents the IR-active vibrational oscillator strengths of the associated phonon modes. It can be seen from Eq. (27) that when $\text{Re}(\epsilon_2) = -1$, a small imaginary component will give a larger energy density due to the reduced loss.

3.4.1. Wavevector dependence of EM-LDOS $\rho(z, \omega)$

The drastic differences in $u(z, \omega, T)$ between the far- and near-field regimes have their origin in different contributions from various in-plane wavevector k_{\parallel} . This effect can be seen in a plot of the k -vector dispersion of the EM-LDOS in Fig. 9 for the three materials.

In the far-field (i) ($z \gg \lambda$, $k_{\parallel} < k_0$), the materials act as broadband emitters with decreased emissivity associated with increased reflectivity. This relationship corresponds to $k_{\parallel} < k_0$ for far-field emission with k_0 representing the free space wavevector. In the transition from the far- to the near-field (ii), the contributions to the total EM-LDOS from states with large in-plane wavevector components k_{\parallel} begin to become significant.

Under conditions for surface wave excitation (Eq. (29)), enhancement of the EM-LDOS associated with evanescent fields begins near $z \simeq \lambda$. Here, states with k_{\parallel} satisfying the polariton dispersion relation (Eq. (28)) start to become the principle contributions to the EM-LDOS. In close proximity to the surface ($z \ll \lambda$), the EM-LDOS lies in the quasi-static regime where it is dominated by large in-plane wavevector states ($k_{\parallel} \gg k_0$) at frequencies where $\text{Im}(\epsilon_2)$ is maximal or the surface polariton resonance condition $\text{Re}(\epsilon_2) = -1$ is met as can be seen from Eq. (27).

This behavior is shown specifically for materials without (Fig. 9a: PTFE) and with (Fig. 9b, c: SiC and SiO₂) SPhP excitation. The three distances above the surface of 10, 1, and 0.1 μm in the plots represent the far-field, transitional, and quasi-static near-field regimes, respectively. In the far-field regime, $\rho(z = 10 \mu\text{m}, \omega)$ is dominated by states below the light line (white dashed) where k_{\parallel} corresponds to propagating modes. The near-field regime is characterized by k_{\parallel} above the light line representing evanescent fields. The magenta lines show $k_{\parallel}(\omega)$ which satisfies the SPhP dispersion relation.

In Fig. 9a the EM-LDOS of PTFE is shown as an example of a material with non-dispersive local molecular excitations. In the far-field (i) it exhibits characteristic broadband emission with only slight dips in $\rho(z, \omega)$ on resonance. As the conditions necessary for the existence of a surface phonon polariton are not met, near-field enhancement is only associated with $\text{Im}(\epsilon_{\text{PTFE}})$ which peaks at the resonance frequencies of the molecular vibrations (ii, iii).

In contrast, for SiC (Fig. 9b) (with similar results for SiO₂ in Fig. 9c), the enhancement of $\rho(z, \omega)$ is governed by the dispersion relationship for the SPhP. As a result, the peak magnitude of $\rho(z, \omega)$ is over one order of magnitude larger for SiC and SiO₂ as compared to that for PTFE. For SiC, as seen at a distance of 10 μm (i), the characteristic gap in the far-field propagating states ($k_{\parallel} < k_0$) beginning at

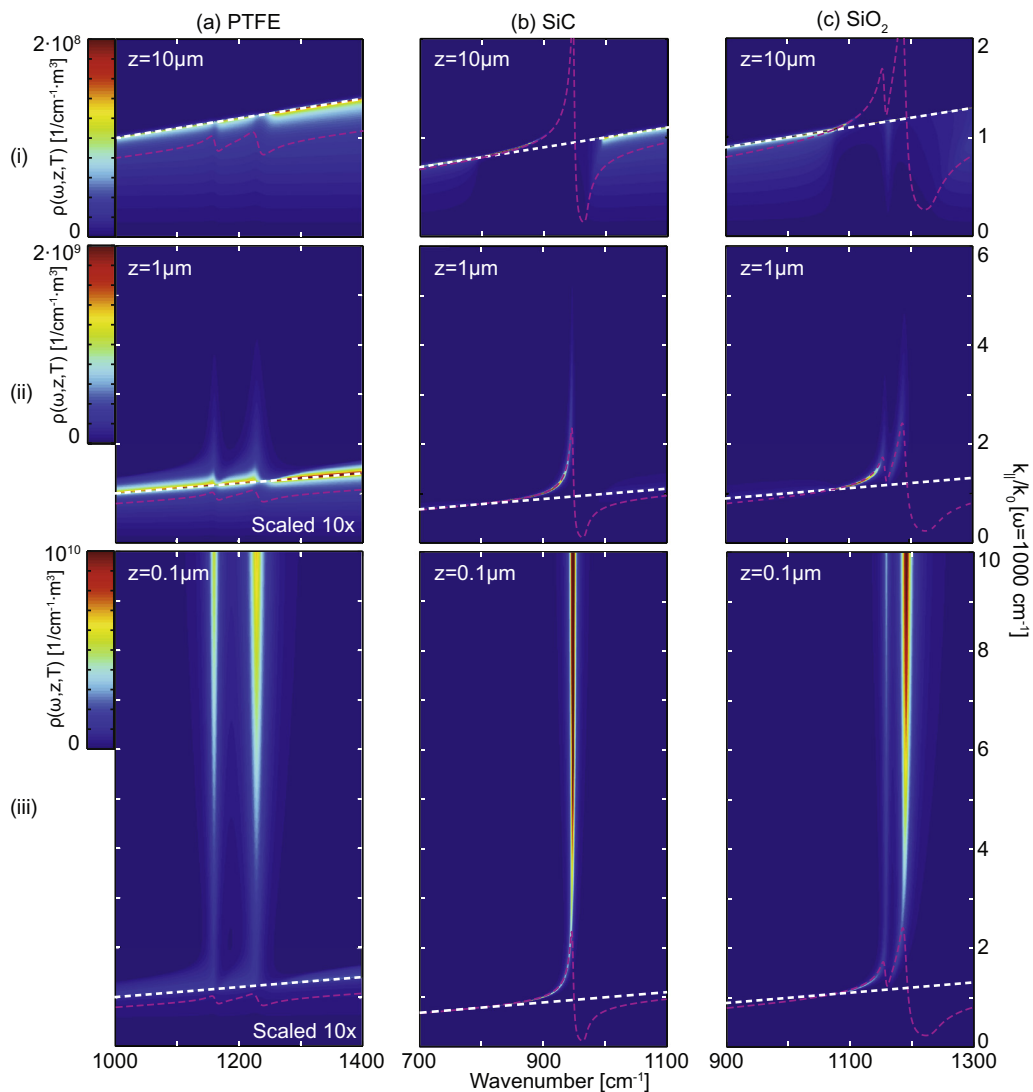


Fig. 9. Calculated in-plane wavevector dependence of the local electromagnetic density of states (EM-LDOS) $\rho(z, \omega)$ above a surface for PTFE (a), SiC (b), and SiO₂ (c) for the far-field (i), transitional (ii), and quasi-static near-field (iii) regimes represented by heights of 10, 1, and 0.1 μm respectively. The free-space light line dispersion (white dashed) marks the far (below) to near-field (above) transition. The surface wave dispersion relations for the materials (dashed magenta) indicate the surface resonance conditions. After Ref. [47]. (For interpretation of the references to color in this figure legend, the reader is referred to the web version of this article.)

1000 cm^{-1} is related to the high-reflectivity Reststrahlen band. In the transition regime at a distance of $1\ \mu\text{m}$ (ii), an enhancement at energies below the SPhP resonance of 950 cm^{-1} following the surface wave dispersion relation develops. At short distances (iii) the distribution of EM-LDOS is governed by high wavevector contributions located at the asymptote of the dispersion relation corresponding to the condition for SPhP excitation.

Similarly, SiO₂ at a distance of $10\ \mu\text{m}$ (i) above the surface exhibits only a slight reduction in the phase space associated with greater reflectivity between ≈ 1050 and $\approx 1250\text{ cm}^{-1}$. Transitioning to a

height of 1 μm (ii), an enhancement associated with the matching of the SPhP condition is observed. As with SiC, at short distances (iii) the distribution of EM-LDOS is governed by high wavevector contributions located at the asymptote of the SPhP dispersion relation which for SiO_2 occurs at $\approx 1157\text{ cm}^{-1}$ and 1190 cm^{-1} . These characteristic strong SPhP related peaks in the EM-LDOS are responsible for the distinct spectral characteristics between the near-field and the far-field regime of SiC and SiO_2 as compared to PTFE.

3.4.2. Distance dependence of spectral energy density $u(z, \omega, T)$

In the previous section we discussed the spectral behaviors of $u(z, \omega, T)$ of different materials. Here we further analyze the details of the distance dependence for SiC as an example.

Fig. 10a shows the drastic increase in $u(z, \omega, T)$ with decreasing distance z . Note the logarithmic scale and the 8 order of magnitude increase of $u(z, \omega, T)$ at the SPhP resonance. Fig. 10b shows the corresponding distance dependencies of $u(z, \omega, T)$ on the SPhP resonance at $\omega = 950\text{ cm}^{-1}$ (red), and off-resonance at $\omega = 1200\text{ cm}^{-1}$ (green) and $\omega = 2000\text{ cm}^{-1}$ (blue), respectively. It can be seen that with increased detuning from resonance, the onset of the near-field $u(z, \omega, T)$ occurs at shorter and shorter distances from the surface, due to the decrease of the long-range SPhP contribution to the field. However, both on- and off-resonant behavior of $u(z, \omega, T)$ have the same slope in the quasi-static near-field region close to the surface, consistent with the $1/z^3$ scaling given by the quasi-static approximation in Eq. (27).

3.5. Spatial and temporal coherence

The theory discussed in the previous section predicts sharp spectral peaks in the vibrationally resonant thermal near-field (see Fig. 8). The narrow linewidths in the near-field spectrum given by intrinsic resonant lifetimes implies a high degree of temporal coherence of the near-field. In contrast, the characteristic linewidth of the blackbody spectrum is on the order of the peak wavelength of the emitted radiation. Though all emission sources have a finite coherence length, a large coherence in thermal radiation may seem surprising since the origin of the field is in random uncorrelated microscopic thermal excitations. The coherence of the near-field is a manifestation of the Fourier filtering performed by vibrational resonances in the medium. The Fourier spectrum of the underlying thermal excitations is that of the black-body distribution, but since the vibrational modes in the material respond more effectively to the fluctuations matching their resonant frequencies, the corresponding excitations are enhanced. These resonantly enhanced thermal excitations are dipolar in nature, producing evanescent EM-fields that decay as $1/z^3$. Since the radiating fields decay as $1/z$, the evanescent field will dominate in the near-field of a resonant material,

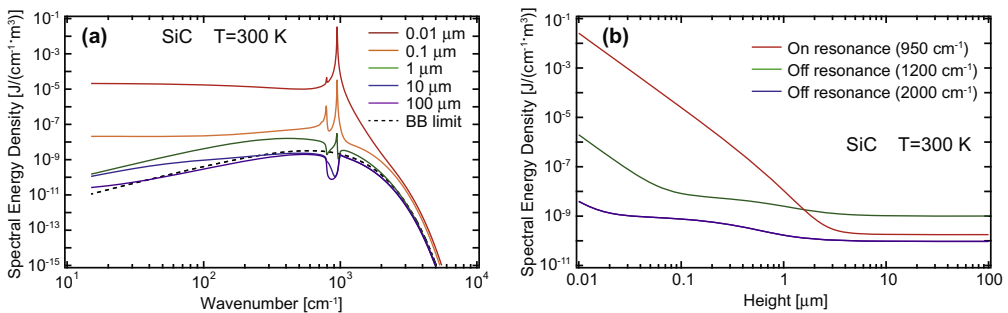


Fig. 10. Distance dependence of $u(z, \omega, T)$ for SiC at $T = 300\text{ K}$ as an example. (a) Changes in the magnitude and spectral distribution of the spectral energy density $u(z, \omega, T)$ as a function of height z . (b) Scaling of $u(z, \omega, T)$ for SiC for three frequencies on and off the SPhP resonance.

causing strong surface confinement of the resonantly enhanced spectral components in the energy density $u(z, \omega, T)$.

Another consequence of the fast $1/z^3$ decay of the resonantly enhanced spectral components is that with decreasing height above the surface, the contribution to energy density is more and more confined to the volume at the surface. This decrease in volume reduces the linewidth and increases the temporal coherence. In the limit of a single oscillator, the linewidth is limited only by the homogeneous lifetime of the oscillator, while an ensemble will have inhomogeneous broadening. This idea, and how measurement techniques can affect the observed linewidth, will be discussed further in Section 4.5.

With increasing distance from the surface, the radiating components start to dominate, and, as seen in Fig. 8, the energy density smoothly evolves into the broad far-field spectrum, with decreasing temporal coherence. This loss of coherence can be prevented by imparting momentum to the near-field by, e.g., a grating structure [48] or a sharp tip (see Section 4), akin to the coupling of electromagnetic modes in a waveguide to propagating radiation. This approach has been demonstrated for SiC to obtain narrow spectral emission in the Reststrahlen band of SiC by grating coupling [48] and tip-scattering [47].

Another related effect of the thermal near-field of resonant materials is its spatial coherence. This is due to long-range interactions on the surface of a material driven by propagating surface waves. As a result, this effect is limited to materials that support surface polaritons, and excludes molecularly resonant materials, or single particle excitations in general.

Spatial coherence can be thought of as a correlation between a local excitation and its corresponding fields acting at another point on the surface. A thermally excited dipole near the surface can generate surface polariton waves that will propagate away from the dipole. These generated EM surface waves will have a fixed spatial phase relationship with respect to their source, and are thus correlated with the initial excitation. These surface waves will interact with nearby excitations, and by summing contributions from all other surface excitations, a correlation length may be determined. The correlation length is limited by the propagation length of the excited surface wave, though in real materials, the coherence length will be further limited by, e.g., scattering processes, defects, or absorption. Since this effect is driven by surface polariton waves, the spatial coherence is confined to the near-field region of the surface, like the aforementioned temporal coherence.

In order to quantify the spatial coherence of the electric field, we can separate the spatial and frequency dependence of the correlation function defined in Eq. (18):

$$\mathcal{E}_{ij}(\vec{r}, \vec{r}', \omega, \omega') = \langle E_i(\vec{r}, \omega) E_j^*(\vec{r}', \omega') \rangle = W_{ij}^E(\vec{r}, \vec{r}', \omega) \delta(\omega - \omega') \quad (30)$$

where \overline{W}^E is called the electric field cross-spectral density tensor. It has an integral expression in terms of the Green's dyadic function given in Eq. (15) (see Ref. [38]). If the electric fields at \vec{r} and \vec{r}' are correlated and in-phase, $\overline{W}^E \neq 0$, and if the fields are uncorrelated or $\pi/2$ out-of-phase, $\overline{W}^E = 0$.

Evaluation of an in-plane component of \overline{W}^E is shown in Fig. 11a, b (from Ref. [38]). The resulting curves exhibit a sinusoidal behavior as the spatial contributions go in and out of phase with the source. The amplitude of sinusoids decay as the energy of the excitation is lost due to, e.g., absorption in the material. Calculations at different wavelength ranges are used to demonstrate the role of propagating surface waves as the origin of the coherence. For wavelengths that support a material polariton resonance, ($\lambda = 620$ nm for Au and Ag and $\lambda = 11.36$ μm for SiC), correlations persist. This is in contrast with wavelengths that do not support propagating surface polariton waves ($\lambda = 620$ nm for W, and $\lambda = 9.1$ μm for SiC). The calculations are all performed at a distance $z = 0.05\lambda$ above the surface where surface-polariton evanescent field contributions dominate. The characteristic decay length of W_{xx}^E defines a coherence length over which the correlations are maintained.

When considering only the propagating far-field, the coherence length is found to be on the order of the wavelength λ [49], consistent with the well-known result of blackbody radiation. However, in the near-field, coherence lengths can be much shorter, or much longer in resonant materials [38]. As an example, for tungsten, a metal which does not support SPPs in the visible spectrum, the coherence length is on the order of $\sim 0.06\lambda$ (close to the value of the skin depth) for a wavelength of 620 nm [38]. This very short length is due to the strong interband absorption and the resulting short penetration

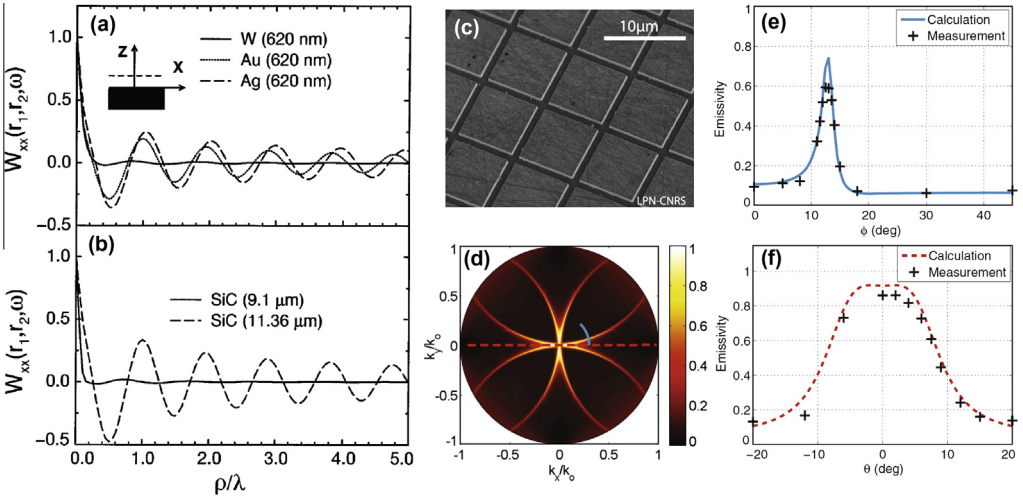


Fig. 11. Frequency dependent electric-field cross-spectral density tensor $W_{xx}^E(\vec{r}_1, \vec{r}_2, \omega)$, a measure of the spatial correlation of the electric field near the surface of a material, calculated at a distance 0.05λ from the surface. Here, $\lambda = 2\pi c/\omega$ and $\rho = \sqrt{|\vec{r}_1|^2 + |\vec{r}_2|^2}$. (a) For metals that support SPPs at $\lambda = 620$ nm (Au, Ag), the correlation is higher than for materials that do not support SPPs at that wavelength (W). (b) Similarly, SiC exhibits a strong spatial correlation at wavelengths that support SPPs, and almost none where SPPs are not supported [38]. (c) SEM image of a SiC double grating structure [50]. (d) A plot of the calculated k -space distribution of emitted intensity at $12.1 \mu\text{m}$ from the SiC double grating pattern. The arc patterns show the high emission when the SPPs are efficiently coupled to free space. (e) $\phi = 0$ and (f) azimuthal angular dependence cross-sections of plot (d), with experimental data. Figure from Refs. [38,50].

depth of the optical field into the metal at that excitation energy. In contrast, for e.g., lossy glass ($1/e$ decay in ~ 1 mm) the coherence length assumes the value of a blackbody $\lambda/2$, with the losses again preventing large scale correlations.

The coherence length in materials supporting surface-polariton resonances can be dramatically increased near the resonant frequencies resulting in near-field correlation lengths on the order of the propagation length of the surface wave. A propagating surface wave allows for long-range spatial interactions at the surface of the medium, with the decay length of a surface wave limiting the length scale over which the field can stay correlated. For SiC near the SPhP resonance, the coherence length is $36\lambda \approx 400 \mu\text{m}$ [38].

Spatial coherence only appears in the near-field and has the same origin as the temporal coherence: the $1/z^3$ dominance of the surface wave contribution to the energy density. Thus, as before, the spatial coherence is lost in the far-field emission. However, if momentum is imparted on these surface waves, the spatial coherence may be preserved. A grating structure or tip may be used to efficiently scatter the surface near-fields into propagating far-field radiation.

By coupling the spatially correlated near-field to propagating far-field, the resulting emission can be made to constructively interfere in a certain direction. The result is a directional emitter, which has been demonstrated using various resonant materials [51–53], e.g., a grating structure on SiC (Fig. 11c) [50]. This gives rise to directional emission in both s- and p-polarizations as determined by the SP dispersion relation, and the momentum imparted by the coupling process. The modeled s-polarized emission in Fig. 11d exhibits this momentum exchange with arcs of high emission intensity where the modes are most efficiently coupled to free space. Fig. 11e, f shows the good agreement with theory of the $\phi = 0$, and azimuthal angular dependence line cuts, respectively, of the data from Fig. 11d.

This spatial correlation is material dependent and, in general, not broadband. As its origin is resonant surface-polariton waves, the fields will only be correlated at certain frequencies where surface waves are permitted. Thus, a broadband directional emitter would be difficult to realize.

4. Thermal infrared near-field spectroscopy (TINS)

4.1. Measurement of thermal near-field radiation

As discussed above, the recent theoretical work on the electromagnetic thermal near-field has predicted fundamentally distinct spectral, spatial, and coherence properties at sub-wavelength dimensions [2,36,54]. One of the most fascinating results of these recent theoretical predictions [2,36,54,55] is the *resonant enhancement* of the near-field spectral energy density when associated with either intrinsic electronic and vibrational excitations, or extrinsic geometric resonances of a medium. Despite its influence on (and possibility for control of) the above phenomena via resonant interaction, experimental investigations of the spectral distribution of the electromagnetic thermal near-field have remained difficult due to its purely evanescent character [56–61].

Perturbing the evanescent field by scattering with a small particle as illustrated in Fig. 1 can project the EM-LDOS into detectable far-field radiation. This near-to-far field coupling is analogous to evanescent field scattering in, e.g., frustrated total internal reflection. By scattering with a non-resonant, point-like particle, the spectral content of the EM-LDOS is expected to be only minimally perturbed. With the radius a of the scatterer, wavevector components up to $k \approx 1/a$ can be probed to first approximation.

Analogously, using a sharp tip as a scatterer in a scanning probe microscope (see also Fig. 1), simultaneous spatial and spectral information can be obtained. As an approach most readily applicable in the IR spectral range, this derived technique of thermal infrared near-field spectroscopy (TINS) is an extension of scattering-scanning near-field optical microscopy (*s*-SNOM) that can probe the evanescent thermal near-field. Using TINS, the enhanced and spectrally narrow resonant evanescent fields associated with different molecular vibrational and surface phonon polariton modes can be characterized.

4.2. Scattering-type scanning near-field optical microscopy (*s*-SNOM)

A typical experimental TINS layout is shown in Fig. 12. The system is based on an atomic force microscope (AFM) preferably operating in non-contact dynamic force mode and ideally allows for independent control of sample and tip temperature. The thermal evanescent fields induced via sample or tip heating [59,60] are scattered by the AFM tip into detectable far-field radiation. This thermal radiation is collected using appropriate high numerical aperture (NA) IR reflective or refractive optics such as a Cassegrain-type reflective objective, an off-axis parabolic mirror (typical NA = 0.5), or IR transparent lenses. For interferometric detection, the tip-scattered radiation is directed through a Michelson interferometer, and detected by an IR detector such as a mercury-cadmium-telluride (MCT) or bolometer detector, depending on the desired detection range (typically 3–20 μm). This spectral range is limited by detector sensitivity, bandwidth of optics, and (on the short wavelength side) maximum achievable sample/tip temperatures.

Discrimination of the near-field signal against the far-field emission and scattering background can most effectively be achieved by lock-in filtering on the frequency of the AFM tip-dither frequency ν_d and its harmonics [62,63]. Due to the non-linear tip-sample distance dependence of the tip-scattered near-field signal, a signal frequency comb at the harmonics of ν_d is generated ($n\nu_d$, $n = 1, 2, \dots$). With increasing harmonics the near-to-far-field contrast increases, though at the expense of signal intensity and ultimately signal-to-noise ratio. Typically detection at the fundamental ν_d or second-harmonic $2\nu_d$ is adequate for near-field discrimination. A resistive heater controls the sample temperature in the 300–500 K range with the upper limit set by stable AFM scanning conditions. The use of specially designed AFM probes (e.g., Anasys Instruments, AN2-200) allows for resistive tip heating up to ≈ 700 K (Fig. 12c). These probes have been further modified by focused-ion beam milling for free line of sight optical access to the tip-sample apex region.

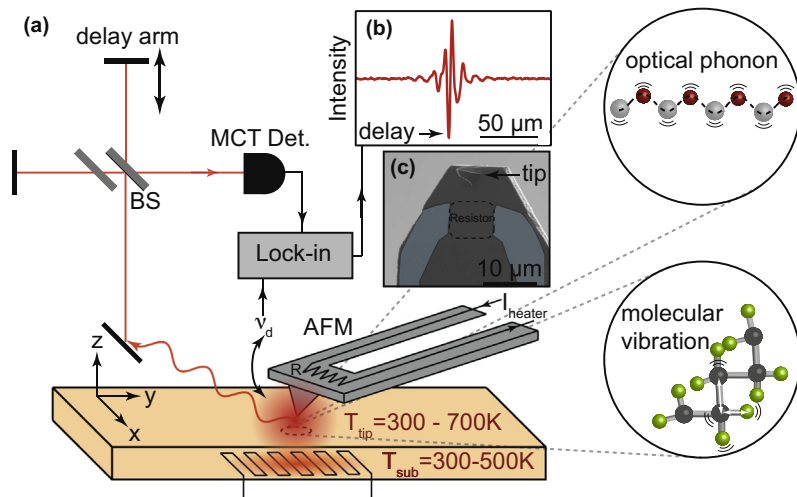


Fig. 12. (a) Experimental setup for thermal infrared near-field spectroscopy (TINS) with thermal near-field radiation scattered by the tip and spectrally resolved via a Michelson-type FTIR interferometer. (b) A typical interferogram acquired via lock-in detection at the AFM tip-dither frequency ν_{dt} . Both the surface or a specialized AFM tip (c) can be heated resistively with the tip in dynamic force feedback. The evanescent thermal near-field exhibits resonant enhancement via molecular or phonon resonances. Figure after Ref. [47].

The advantage of the use of heated AFM probes is that they allow for stable scanning conditions to be maintained with higher temperatures in the tip-sample gap region compared to either sample heating or active heating of both tip and sample. Heated probes provide a local heat source which is advantageous in studying samples which would degrade subjected to substrate heating, and allows for higher achievable temperatures. Substrate heating provides a more uniform sample temperature, yet at the expense of a much larger far-field background. With the heated AFM tip in close proximity to the material, local heat transfer occurs via ballistic thermal air conduction [64]. Localized surface melting of, e.g., polycarbonate samples, is used to estimate the surface temperature near the tip. As an example, for a nominal tip temperature of $T_{tip} = 700$ K, at least $T_{sample} \approx 550$ K surface temperature with the AFM operating in non-contact force feedback mode can readily be obtained. Given the narrow linewidth of IR vibrational resonances compared to the overall blackbody spectrum, the exact knowledge of the surface temperature is not critical. Surface temperature primarily affects the signal intensity, and only to a minor extent the spectral characteristics of the vibrational near-field energy density distribution. Care needs to be taken, however, with regards to the interpretation of TINS spectra when tip and sample are at different temperatures yet coupled through their respective near-field modes (See section 4.5 below).

4.3. Thermal infrared near-field spectroscopy: phonon-polariton and molecular resonances

The spectrum of the scattered thermal light from the heated tip-sample gap region is obtained from the detected interferogram via Fourier transform. With the use of a dielectric tip material (e.g., Si/SiO₂), which is off-resonant and thus spectrally broadband in the vibrational spectral range of interest, the tip-scattered light reflects the intrinsic or extrinsic vibrational/phonon resonances of the sample [36,65].

Fig. 13 (a–c, red lines, upper panels) shows the tip-scattered thermal near-field signal from samples of SiC, SiO₂, and PTFE, respectively, using a heated tip at $T_{tip} \approx 700$ K. For all three materials peaked near-field spectral signal distributions are observed associated with the respective molecular or surface phonon polariton (SPhP) resonances. For comparison, the expected spectral energy density distribution $u(z, \omega, T)$ at 20 nm above the surface is calculated for the three materials using literature values

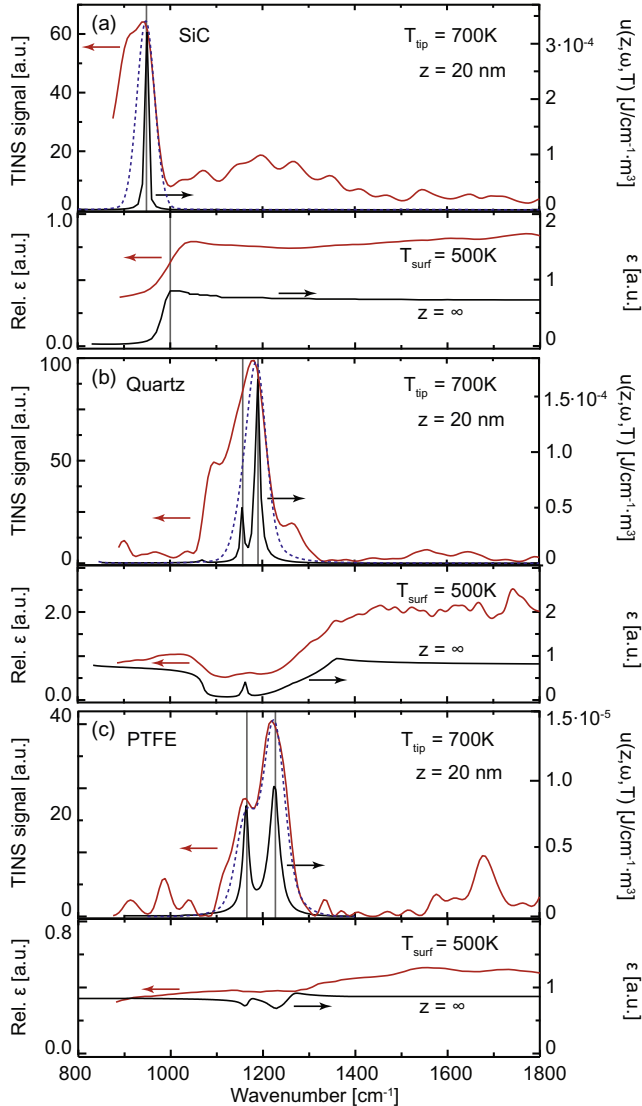


Fig. 13. Tip-scattered thermal near-field spectra (upper panels, red lines, a–c) for SiC, SiO₂, and PTFE, associated with the characteristic phonon-polariton, and molecular vibrational resonances. The spectral energy density associated with the EM-LDOS (upper panels, black lines, a–c), calculated for $z = 20$ nm and $T = 500$ K, is displayed concurrently with the simulated spectral distribution of the TINS signal (blue dashed lines, a–c, arbitrary units). In contrast, far-field thermal emission from heated substrates with the tip far retracted (lower panels, red lines, a–c) exhibit signal decreases associated with elevated reflectivity on resonance in agreement with calculated far-field thermal emissivity given by Kirchhoff's law (lower panels, black lines, a–c). Figure after Ref. [47]. (For interpretation of the references to color in this figure legend, the reader is referred to the web version of this article.)

for the respective complex dielectric function (a–c, black lines, upper panels) [42,33] using the exact solution presented in Section 4.5 (i.e., not using the quasi-static approximation). The corresponding relative far-field thermal emission spectra from the three heated materials measured with the AFM tip retracted are shown (a–c, red lines, lower panels) normalized against emission from a Si surface. They exhibit a signal *decrease* near the respective resonances in accordance with Kirchhoff's law of

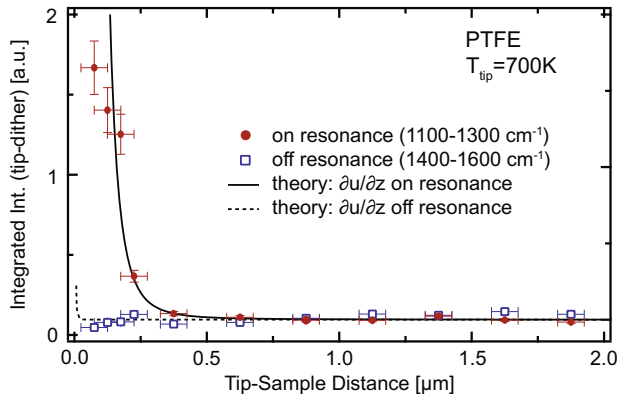


Fig. 14. Distance dependence for the integrated measured spectral intensity on- (1100–1300 cm^{-1}) and off-resonance (1400–1600 cm^{-1}) for PTFE in comparison to corresponding model calculations (solid and dashed lines). This result confirms strong near-field localization. Figure after Ref. [47].

thermal emission for opaque bodies (Fig. 13a–c, black line, lower panels) [40]. As can be seen for SiC, a peaked near-field signal occurs near $\sim 945 \text{ cm}^{-1}$; for SiO_2 it is observed between 1150 cm^{-1} and 1205 cm^{-1} . These spectral peaks correspond to the SPhP resonance modes of the respective materials. The SPhP resonance condition is met in SiC at $\sim 950 \text{ cm}^{-1}$ while for SiO_2 it is met both at $\sim 1157 \text{ cm}^{-1}$ and $\sim 1190 \text{ cm}^{-1}$ for the planar material/air interface. As a non-dispersive molecular solid PTFE does not meet the conditions for surface wave excitation. Its distinct molecular resonances located at 1158 , 1210 , and 1240 cm^{-1} (latter two spectrally not resolved) are associated with the different C–F symmetric ω_S and antisymmetric ω_{AS} vibrational stretch modes [43,44]. The measured signal magnitude is weaker compared to that from polaritonic materials, as expected.

The linewidths in the tip-scattered near-field signal are larger than the corresponding peaks in the calculated energy densities. This is in part due to the finite resolution of the experiment. The blue dashed lines in Fig. 13a–c simulate the expected broadening due to this effect. The origin of additional broadening in SiC and SiO_2 is discussed further in Section 4.5.

As discussed theoretically above in Section 3.4, the observed resonant spectral near-field characteristics are fundamentally distinct from the manifestation of these resonances in far-field emission, scattering, and reflection. SiC exhibits a reduction in far-field emissivity below $\sim 1000 \text{ cm}^{-1}$ which marks the onset of the high reflectivity Reststrahlen band (800 – 1000 cm^{-1}). The measured emission from SiO_2 shows slight dips corresponding to enhanced reflectivity associated with the series of LO and TO Si–O phonon modes (1050 – 1250 cm^{-1}) [45,46]. The PTFE film further exhibits reduced emissivity in the vicinity of the C–F vibrational modes, albeit weaker, due to the lower vibrational density of states compared to that of the optical phonon modes in SiC or SiO_2 .

4.4. Distance dependence

Measurements as a function of distance above the sample surface serve to verify the near-field origin of the spectral behavior observed. As an example the corresponding tip-sample distance dependence of the integrated combined ω_S and ω_{AS} modes for PTFE (1100 – 1300 cm^{-1}) is shown in Fig. 14 (red solid circles). A strong near-field confinement for distances below $\sim 200 \text{ nm}$ is found. The corresponding parameter-free on-resonance model calculation of the distance dependence of the expected TINS signal derived from the spectral energy density $u(z, \omega, T)$ for PTFE is shown as the solid line.⁷ In contrast, the off-resonant signal contribution (here integrated from 1400 to 1600 cm^{-1})

⁷ With the scattered power of the tip $P_{\text{scat}}(z, \omega, T) \propto u(z, \omega, T)$, we model the distance dependence of the TINS signal occurring at a tip-dither frequency of ν_d as proportional to the quantity $\partial u / \partial z$ as the signal in dynamic *s*-SNOM measurement is primarily sensitive to the gradient of the optical near-field (see Ref. [66]).

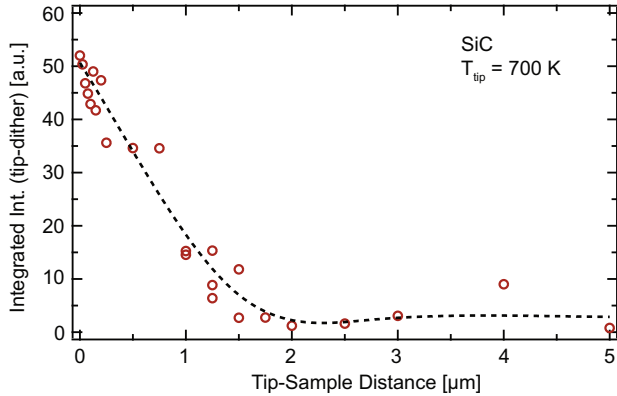


Fig. 15. Distance dependence of the spectrally integrated resonant TINS signal ($925\text{--}975\text{ cm}^{-1}$) of SiC. Onset of the signal increase is seen at a height of $z \approx 1.5\text{ }\mu\text{m} \approx \lambda/2\pi$. An interpolation (black dashed line) of the approach data is provided as a guide to the eye. Figure after Ref. [47].

does not exhibit a discernible increase (blue open squares) within the uncertainty of the experiment. This behavior is in agreement with the corresponding off-resonant calculation (dashed line) which only exhibits a small increase at very short distances ($<50\text{ nm}$) [2,36]. Fig. 15 shows the corresponding data for SiC. From the spectral energy density $u(z, \omega, T)$, an onset of signal increase is observed associated with the SiC surface phonon polariton (SPhP) resonance at $\omega \approx 950\text{ cm}^{-1}$ ($\lambda \approx 10.5\text{ }\mu\text{m}$) at a height of $z \approx 1.5\text{ }\mu\text{m}$ corresponding to $\sim \lambda/2\pi$. Here, a less pronounced enhancement is observed than expected from the $u \propto z^{-3}$ scaling compared to PTFE. Those differences and the details in tip-sample distance behavior are not yet well-understood, but could be due to details in the heat transfer between the tip and surface. However, both results qualitatively show the near-field localization and spectral enhancement of the resonant thermal near-field.

4.5. TINS modeling: tip-sample coupling

The origin and consequences of the difference between the far- and near-field spectral behavior, its distance dependence, and its material specific resonant and non-resonant relationship with molecular vibrations, optical phonons, or surface polariton modes can be understood from an in-plane wavevector k_{\parallel} dependent analysis of the spectral distribution of the EM-LDOS calculated using Eq. (24) and displayed in Fig. 9 above.

To understand the general relationship between the tip-scattered thermal near-field signal and the underlying EM-LDOS, one has to consider that the detected near-field signal can be affected by the mutual optical polarization between the tip and the sample. Similar to conventional *s*-SNOM with external illumination, the radiating polarization of the tip is driven by the thermal evanescent field of the sample which in turn is affected by the presence of the tip. Modeling the tip as a small off-resonant polarizable sphere (shown schematically in Fig. 16a), its effective polarizability as a function of distance above the surface z and radius r is given by

$$\alpha_{\text{eff}} = \alpha \left(1 - \frac{\alpha\beta}{16\pi r^3 \left(1 + \frac{z}{r}\right)^3} \right)^{-1}. \quad (31)$$

$\beta = (\epsilon_2 - 1)/(\epsilon_2 + 1)$ quantifies the strength of the virtual image dipole in the surface. $\alpha = 4\pi r^3 \cdot (\epsilon_{\text{sph}} - 1)/(\epsilon_{\text{sph}} + 2)$ is the Clausius–Mossotti relation for the polarizability of a sphere with frequency dependent dielectric permittivity ϵ_{sph} [62,63]. The resulting optical polarization leads to a spectral distribution of the scattered power which can to a first approximation be expressed as the product of $u(z, \omega, T)$, the effective scattering cross-section of the sphere C_{eff} , and the speed of light c as,

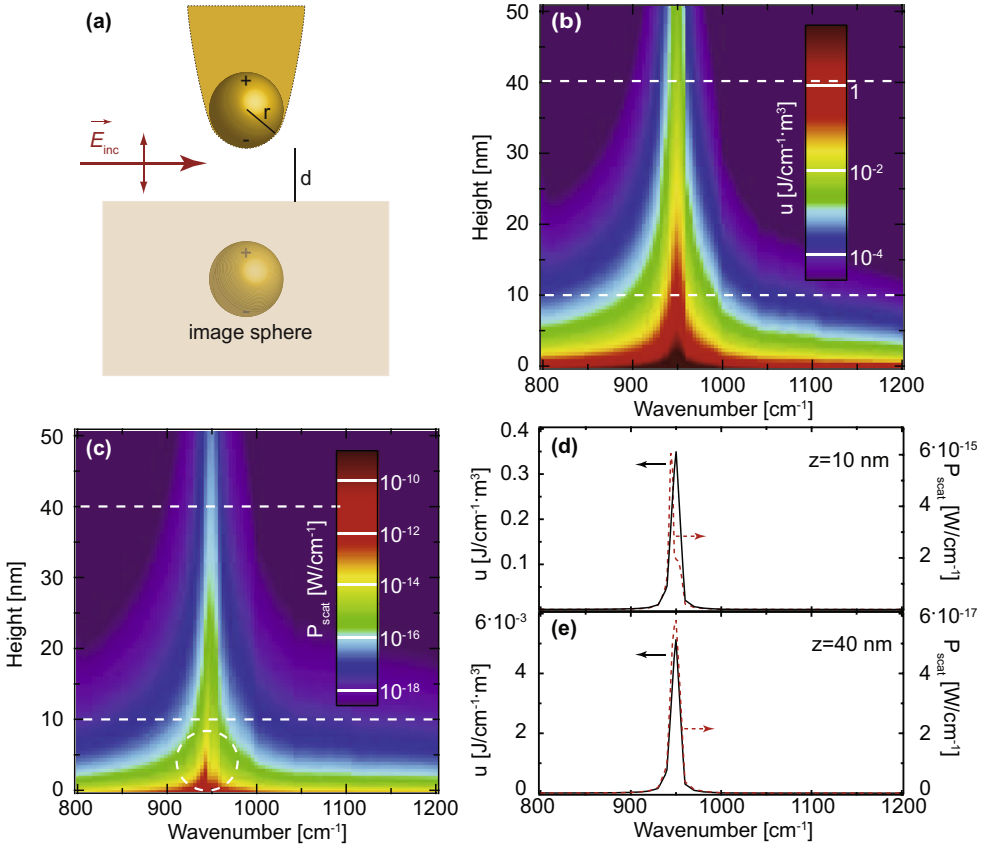


Fig. 16. (a) Modeling the tip as a spherical dipole. The height and spectral dependence of $u(z, \omega, 500 \text{ K})$ (b) and $P_{\text{scat}}(z, \omega, 500 \text{ K})$ (c) are displayed with logarithmic color scales as calculated using Eqs. (24) and (32) for a Si sphere of radius $a = 20 \text{ nm}$. The white dashed circle in (c) indicates the $5\text{--}10 \text{ cm}^{-1}$ red shift predicted at distances less than the apex radius. Panels (d) and (e) compare the spectral distributions of $u(z, \omega, 500 \text{ K})$ and $P_{\text{scat}}(z, \omega, 500 \text{ K})$ for heights of 10 and 40 nm, marked by the white dashed lines in panels (b) and (c), representing height-to-tip radius ratios of $z/a = 0.5$ and $z/a = 2$ respectively. (For interpretation of the references to color in this figure legend, the reader is referred to the web version of this article.)

$$P_{\text{scat}}(z, \omega, T) = C_{\text{eff}} \cdot c \cdot u(z, \omega, T). \quad (32)$$

Here, the effective scattering cross-section of the sphere C_{eff} is defined in terms of its effective polarizability as $C_{\text{eff}} = k^4 |\alpha_{\text{eff}}|^2 / (6\pi)$ [67]. Note that it is assumed that $u(z, \omega, T)$ itself is unaffected by the presence of the sphere.

As an example, the resulting spectral distribution of the tip-scattered intensity induced by the near-field thermal spectral energy density for $T = 500 \text{ K}$ is plotted in Fig. 13 (blue dashed line) for the three materials convolved with the $\approx 25 \text{ cm}^{-1}$ spectral resolution of the experiment. There is good general agreement between the experimentally observed results and the model. The scattered near-field power derived from the relationships above also agrees well with the 30–100 pW of near-field scattered power observed in those measurements.

The experimental results on SiC are reminiscent of laser based s-SNOM spectroscopic measurements which exhibit a signal peak at 920 cm^{-1} [68,69]. As in s-SNOM, Eq. (32) incorporates optical phase-related few- cm^{-1} red shifts with line asymmetry due to the tip-sample coupling at short distances ($z \lesssim \text{AFM tip apex radius}$) [62,69]. This effect is slightly more pronounced when considering details of tip geometry and higher-order mode coupling compared to the simple model above, but within the limits of the natural line width of a molecular or phonon excitation.

An additional 5–10 cm^{-1} red shift and spectral broadening is also expected from phonon softening and increased damping with temperature [57,70–72]. We attribute these as the dominant effects, together with a higher defect density of the natural quartz measured, for the observed deviations from the model calculations. However, a detailed discrimination is not possible within the available spectral resolution and signal to noise ratio of the experiment.

For distances larger than the tip-sample coupling range (i.e., larger than the apex radius), and in general for sharp non-resonant tips with apex radius $a \lesssim 10$'s of nm, TINS can thus measure the evanescent spectral energy distribution and resonances of the sample to a good approximation with the tip acting only as a weakly perturbing scatterer. The associated underlying near-field EM-LDOS, also for shorter distances, may be explicitly extracted using an appropriate model that incorporates the dynamic variation of coupling with the tip-dither motion, the role of far-field interference and surface reflection, details of the tip geometry affecting coupling and scattering, as well as contributions due to variations in the surface topography. With knowledge of the EM-LDOS calculated using Eq. (24), the spectral energy density above a specific surface material at a given temperature may be calculated by multiplying with the Planck distribution, $u(z, \omega, T) = \rho(z, \omega) \cdot \Theta(\omega, T)$. Fig. 16b displays the resulting $u(z, \omega, T)$ in the near-field regime above a SiC surface in the vicinity of the SPhP resonance frequency at 950 cm^{-1} . The associated scattering by the AFM-tip, modeled by the scattering of a small off-resonant polarizable sphere and calculated via Eq. (32) for a 20 nm Si sphere, is displayed in Fig. 16c. Line-traces displaying the spectral distribution $u(z, \omega, T)$ and the associated spectral scattering power P_{scat} of the tip-sphere at heights of 10 and 40 nm above the surface are displayed in panels Fig. 16d and f, representing height to tip-radius ratios of 0.5 and 2 respectively.

At distances smaller than the AFM tip-radius (panel c, circled region), the effect of mutual coupling between the tip and the sample due to the image dipole coupling of the tip leads to a $\sim 5 \text{ cm}^{-1}$ redshift in $P_{\text{scat}}(z, \omega, T)$. The incorporation of surface reflection terms for the P_{scat} has only minimal effects on its spectral distribution. For heights greater than the tip-radius (panel e), the direct coupling with the surface is minimal, suggesting that the scattering distribution of the non-resonant sphere reflects the intrinsic spectral distribution of $u(z, \omega, T)$.

For a large tip radius ($a \sim \lambda_{\text{Th}}$), the quasi-static approximation breaks down, and significant spectral red-shift and broadening can occur [73]. This effect was modeled by considering retardation effects in the spherical dipole model, and including contributions from multiple tip-sample reflections to the detected signal. In general, this model predicts a red-shift and general broadening in a TINS spectrum for a larger apex radius. These results may also be described using more refined tip-sample coupling models which consider the actual tip geometry in more detail [69]. In recent experiments, a variation in peak position and linewidth is observed above a SiC substrate using tips of different effective apex radii [74]. These results suggest a considerable sensitivity of the spectroscopic details to tip apex geometry. For tips with a large apex radius, few 10's of nm and more, $u(z, \omega, T)$ of the medium itself can be perturbed, in particular for a SPhP supporting medium, as the SPhP resonance condition is no longer that of a medium/vacuum interface. Instead, the interface is that of a medium and an effective medium of vacuum plus tip material.

Another effect on the spectral linewidth in TINS can arise from the possible influence of the tip-scattering probe and near-field coupling on the radiative and non-radiative lifetimes of an excitation. When the tip is brought close to the surface, it can add additional radiative and non-radiative decay pathways that can modify the lifetime of the vibrational excitation. The linewidth of the observed spectra is thereby increased [75] since the decay times of the polarization of, e.g., metallic tips are usually much shorter than those of the vibrational polarization ($T_2^{\text{tip}} \sim 10 \text{ fs} \ll T_2^{\text{vib}} \sim 100$'s fs) [76].

Despite the aforementioned sensitivity of TINS spectral peak positions to extrinsic factors such as apex radius, this effect is specific to strongly resonant materials supporting SPP or SPhP resonances. In that case, different models may be used to separate these effects from the intrinsic material response [69,73,74]. In contrast, molecular resonances are less sensitive to these effects, and the observed peak positions match the intrinsic vibrational mode frequencies. This is because their dielectric function, even for large oscillator strengths, exhibits weaker on resonance dispersion compared to strong phonon modes, which due to the negative $\text{Re}(\epsilon(\omega))$ in certain spectral regions support SPhPs. Further, a sharp dielectric tip at tip-sample distances larger than the apex radius will only minimally perturb

$u(z, \omega, T)$ and its scattered near-field spectral features, thus allowing for quite accurate measurements of the EM-LDOS even for strongly resonant materials.

4.6. TINS as a nano-spectroscopic/nano-imaging technique

As a variant on scattering-type scanning near-field optical microscopy (s-SNOM), TINS is an inherently nano-spectroscopic and nano-imaging technique, with spatial resolution only limited by the tip-apex radius. Fig. 17 shows thermal near-field imaging of a heated SiC–Au test structure [60]. Gold stripes on a SiC substrate were heated to 170 °C and a tungsten tip was scanned in non-contact AFM mode (schematic shown in Fig. 17a). The tip scattered radiation was detected using a MCT detector after spectral filtering the SiC SPhP signal at $\approx 10.9 \mu\text{m}$ with a $1 \mu\text{m}$ bandwidth. Fig. 17b shows a thermal near-field image. A higher signal level above the gold is indicative of the higher EM-LDOS contributions from thermally excited surface plasmon polaritons (SPPs). Fringes parallel to the edge of the stripe are observed with the number of fringes dependent on the width of the stripe, with two dimensional interference patterns observed at the end (Fig. 17d) with SPPs launched in longitudinal and transverse directions. The measured spatial distributions are consistent with simulations of the spatial distribution of the EM-LDOS at a height of $z = 3 \mu\text{m}$, reproduced in Fig. 17c.

The standing SPP modes have been interpreted as spatial coherence of the thermal near-field as discussed in Section 3.5. SPP modes are thermally excited and give rise to a spatial correlation of the thermal near-field polarization. In this structure, the thermally excited SPPs propagate, reflect off the edges, and interfere with counter-propagating SPPs. The stripes act like a cavity where SPPs of a certain wavenumber create a standing wave pattern and result in a spatially-periodic modulation of the EM-LDOS.

Spatio-spectral TINS imaging has been demonstrated using a molecularly resonant sample [47]. The edge of a $\sim 100 \text{ nm}$ thick PTFE flake on a Si substrate was imaged, as shown in Fig. 18. The line trace (f, laterally averaged over 6 lines in the high resolution scans c,d) indicates a spatial resolution of $\sim 50 \text{ nm}$ consistent with the tip apex radius. The enhanced signal at the PTFE edge is due to the enhanced near-field coupling and scattering at the step edge. Using the spatial resolution data obtained from Fig. 18, the sensitivity of the TINS measurement can be estimated for PTFE. Here, for a density of $2.2 \cdot 10^6 \text{ g/m}^3$ and a tip-apex localized sample volume of $\sim 1 \cdot 10^6 \text{ nm}^3$, the number of C-F modes probed amounts to $\sim 5 \cdot 10^7$, corresponding to ≈ 40 attomol of CF_2 groups. Modeling the statistical distribution of the PTFE CF_2 excitations using the micro-canonical partition function for a harmonic oscillator $Z^* = 1/(1 - \exp(-\hbar\omega/k_B T))$, an estimated 3–8% fraction of vibrationally excited oscillators contributes to the signal for temperatures in the 500–700 K range. Assuming a minimal signal-to-noise ratio of ~ 10 necessary for spectral peak assignment the resulting sensitivity for spectroscopic contrast is as high as 3–5 attomol. This sensitivity represents an increase in IR-spectroscopic sensitivity of at least 4 orders of magnitude over conventional far-field IR microscopy techniques where

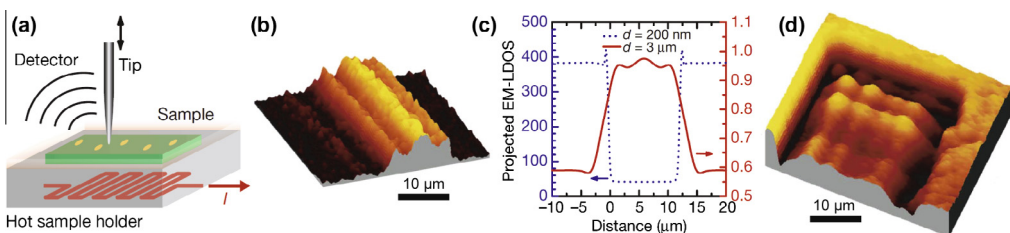


Fig. 17. Spatial mapping of the thermal near-field of a heated surface. (a) A schematic of the experimental set-up. (b) The measured thermal infrared signal on a gold stripe on a SiC substrate with (c) the corresponding calculated density of states at 200 nm (blue curve) and 3 μm (red curve) above the surface. The gold shows a higher signal at $z = 3 \mu\text{m}$ due to the larger surface-normal spatial extent of the SPPs. (d) The end of a gold stripe showing interference patterns in both dimensions. Figure taken from Ref. [60]. (For interpretation of the references to color in this figure legend, the reader is referred to the web version of this article.)

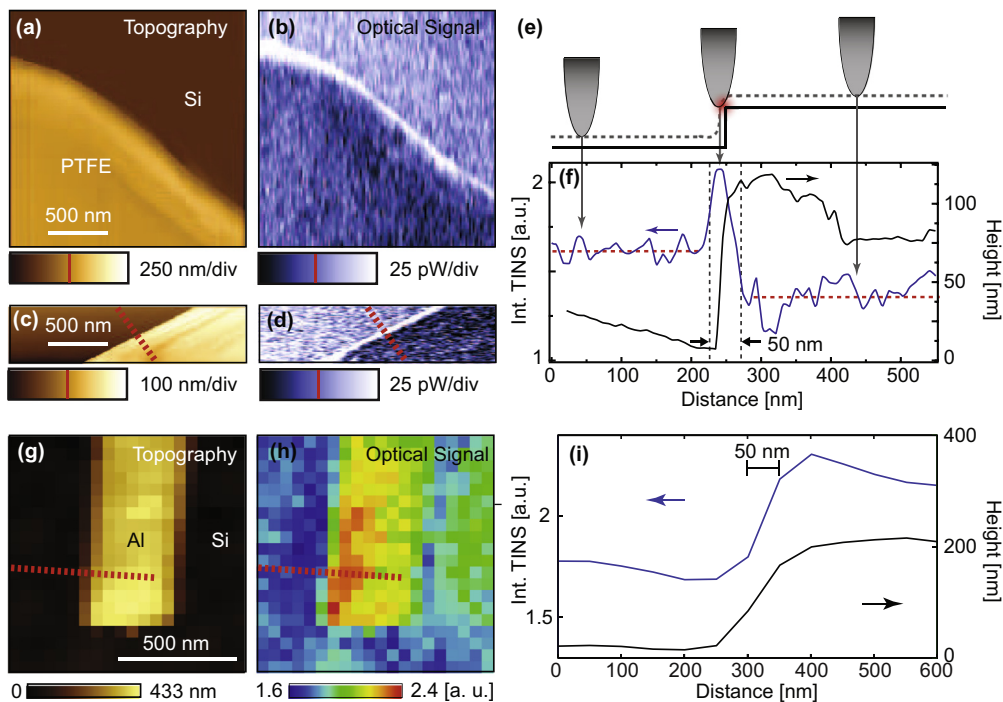


Fig. 18. Topography (a, c) and spectrally integrated TINS signal (b, d) with contrast between a PTFE flake of thickness ~ 100 nm on a Si substrate. Panels (c) and (d) represent a higher resolution scan near the PTFE step edge with line-trace (f) of topography and TINS signal (laterally averaged over 6 scan lines, along red dashed line in (c)). An increase in scattering with the tip at the PTFE step edge is observed as indicated schematically in (e). The spatial resolution of ~ 50 nm as indicated by the vertical gray dashed lines in panel (f) agrees with expectation related to tip apex radius. Panels (g) and (h) represent topography and spectrally integrated TINS images of an Al nano-structure on a Si substrate, with line traces given in panel (i) (along red dashed lines in (g) and (h)). Figures (a–f) after Ref. [47]. (For interpretation of the references to color in this figure legend, the reader is referred to the web version of this article.)

spatial resolution is constrained by the diffraction limit ($\sim 10 \mu\text{m}$) [77] and non-enhanced far-field absorption.

The sensitivity and specificity demonstrated above is comparable to conventional laser-based s-SNOM [78], and can be further improved utilizing IR optical antenna modes of specially engineered tips. This work shows that the enhanced EM-LDOS in the thermal near-field associated with resonance modes enables TINS as a new scanning probe technique with IR vibrational contrast and with spatial resolution determined by the EM-LDOS near-surface localization and/or tip apex radius. TINS, as an implementation of s-SNOM with a heated tip, thus allows for broadband chemical nano-spectroscopy, complementary to the use of an external thermal light-source [79], yet with higher sensitivity and the thermally driven vibrational optical dipoles providing their own intrinsic light source.

5. Heat conduction in the thermal near-field

In this section we will discuss heat conduction in the thermal near-field. Two models closely related to typical micro- and nano-structure geometries are presented, namely heat transfer between two parallel surfaces, and heat transfer between a small point-like particle and a flat surface. Treatment of an arbitrary geometry based on numerical methods such as the scattering matrix approach is also briefly mentioned. Finally, several applications utilizing near-field heat transfer are discussed.

5.1. Heat transfer between two parallel planes

The rate of heat transfer between two planar surfaces can be derived based on fluctuational electrodynamics, which predicts a near-field enhancement [80,81]. The same problem when investigated using a Drude model for the material dielectric function, specifies a distance dependence of the heat transfer $\propto 1/d^2$ at short distances [82].

The radiative heat power transfer rate per unit area Φ (hereafter referred to as the total heat flux) can be derived as follows [5,55,81–84]: the total heat flux between two black plates (held at temperature T_1 and T_2 , respectively, by coupling to a bath) at large separation, is given by the Stefan–Boltzmann law $\Phi = \sigma(T_1^4 - T_2^4)$. In this case, the heat flux is only determined by propagating electromagnetic waves. The Poynting vector averaged over an ensemble of random currents is $\langle S(\vec{r}, \omega) \rangle = 1/2 \text{Re}(\langle E(\vec{r}, \omega) \times H(\vec{r}, \omega)^* \rangle)$. To account for the evanescent contributions at small separation, one needs to evaluate $\langle S(\vec{r}, \omega) \rangle$, which can be expressed as a function of geometric boundary conditions and material properties using $E(\vec{r}, \omega)$ and $H(\vec{r}, \omega)$ written in terms of the Green’s dyadic functions (see Eq. (15)). Due to the correlation between $E(\vec{r}, \omega)$ and $H(\vec{r}, \omega)$, the resulting average does not equal to zero. The corresponding heat flux component at frequency ω is just $q(d, \omega) = \langle S_z(d, \omega) \rangle$. The flux can be written as the sum of two terms $q(d, \omega) = q^{\text{prop}}(d, \omega) + q^{\text{evan}}(d, \omega)$. $q^{\text{prop}}(d, \omega)$ is the contribution from propagating waves,

$$q^{\text{prop}}(d, \omega) = \sum_{q=s,p} \frac{\omega^2}{2\pi^2 c^2} (\Theta(\omega, T_1) - \Theta(\omega, T_2)) \times \int_0^{\omega/c} \frac{k_{\parallel} dk_{\parallel}}{k_0^2} \left(\frac{(1 - |r_1^q|^2)(1 - |r_2^q|^2)}{4|1 - r_1^q r_2^q e^{2ik_{\perp}d}|^2} \right), \tag{33}$$

where $\Theta(\omega, T)$ is the mean thermal photon energy at temperature T . The contribution from evanescent waves $q^{\text{evan}}(d, \omega)$ is

$$q^{\text{evan}}(d, \omega) = \sum_{q=s,p} \frac{\omega^2}{2\pi^2 c^2} (\Theta(\omega, T_1) - \Theta(\omega, T_2)) \int_{\omega/c}^{\infty} \frac{k_{\parallel} dk_{\parallel}}{k_0^2} e^{-2\text{Im}(k_{\perp})d} \left(\frac{\text{Im}(r_1^q) \text{Im}(r_2^q)}{|1 - r_1^q r_2^q e^{-2\text{Im}(k_{\perp})d}|^2} \right) \tag{34}$$

where r_1^q, r_2^q are the Fresnel reflection coefficients for s- ($q = s$) or p-polarization ($q = p$) at both interfaces.

Integrating all the frequency components, the total heat flux Φ between the two media amounts to:

$$\begin{aligned} \Phi(d, T_1, T_2) &= \int_0^{\infty} d\omega q(d, \omega) \\ &= \int_0^{\infty} \frac{d\omega}{\pi} [\Theta(\omega, T_1) - \Theta(\omega, T_2)] \\ &\quad \times \sum_{q=s,p} \left[\int_0^{\omega/c} \frac{k_{\parallel} dk_{\parallel}}{2\pi} \frac{(1 - |r_1^q|^2)(1 - |r_2^q|^2)}{|1 - r_1^q r_2^q e^{2ik_{\perp}d}|^2} + \int_{\omega/c}^{\infty} \frac{k_{\parallel} dk_{\parallel}}{2\pi} \frac{4\text{Im}(r_1^q) \text{Im}(r_2^q) e^{-2\text{Im}(k_{\perp})d}}{|1 - r_1^q r_2^q e^{-2\text{Im}(k_{\perp})d}|^2} \right]. \end{aligned} \tag{35}$$

In the limit of a large separation, the propagating part recovers the expression of the classical Stefan–Boltzmann law. By defining a heat transfer coefficient as

$$h_R(d, \omega) = \lim_{(T_1 - T_2) \rightarrow 0} \frac{q(d, \omega)}{T_1 - T_2}, \tag{36}$$

we can expand the evanescent part asymptotically for short distance to

$$h_R(d, \omega) \simeq \frac{1}{d^2} \frac{\text{Im}(\epsilon_1) \text{Im}(\epsilon_2)}{|1 + \epsilon_1|^2 |1 + \epsilon_2|^2} \times k_B \left(\frac{\hbar\omega}{k_B T} \right)^2 \frac{e^{\hbar\omega/k_B T}}{(e^{\hbar\omega/k_B T} - 1)^2}, \tag{37}$$

with ϵ_1 and ϵ_2 the dielectric functions of the respective media. This expression yields the $1/d^2$ distance dependence of the transfer coefficient and its frequency dependence via $\epsilon_1(\omega)$ and $\epsilon_2(\omega)$. Indeed,

when real part of the dielectric function of one of the media approaches -1 , the radiative heat transfer coefficient exhibits resonant enhancement through surface resonances [2,84–89]. Non-local effects, such as the anomalous skin depth, can also be accounted for by replacing the local dielectric function with a spatially non-local dielectric function [83,90,91].

5.2. Heat transfer between a point-like particle and a planar surface

In a geometry related to a scanning probe experiment, with the tip and a flat sample held at different temperatures, enhanced heat transfer at short distances can occur [92,93]. Heat transfer between a plane and a small particle used as a model of the scanning probe tip was studied under the point dipole approximation, and the heat transfer rate between a hot tip and a cool surface was estimated [55].

The radiative power exchanged between a point-like spherical particle and a semi-infinite substrate can be derived as follows [2,35,94]. The small particle of radius a and dielectric function $\epsilon_p(\omega) = \epsilon'_p(\omega) + i\epsilon''_p(\omega)$ is held at temperature T_p . The particle polarizability is $\alpha(\omega) = 4\pi a^3 (\epsilon_p(\omega) - 1)/(\epsilon_p(\omega) + 2)$. The substrate medium is a homogeneous, isotropic material of dielectric function $\epsilon_B(\omega) = \epsilon'_B(\omega) + i\epsilon''_B(\omega)$ and held at temperature T_B . The particle is at a distance d above the interface.

The power absorbed by the particle when subject to the field of the half-space substrate is given by

$$P_{abs}^{B \rightarrow P}(\omega) = \frac{2}{\pi} \frac{\omega^4}{c^4} \text{Im}(\epsilon_B(\omega)) \text{Im}(\alpha(\omega)) \Theta(\omega, T_B) \sum_{ij} \int_B |G_{ij}^E(\vec{r}_p, \vec{r}', \omega)|^2 d^3 \vec{r}'. \quad (38)$$

This expression can be expanded asymptotically by evaluating the Green's function, and the resulting expression of the power absorbed is given by

$$P_{abs}^{B \rightarrow P}(d, \omega) \simeq \frac{1}{4\pi^2 d^3} 4\pi a^3 \frac{3\epsilon''_p(\omega)}{|\epsilon_p(\omega) + 2|^2} \frac{\epsilon''_B(\omega)}{|\epsilon_B(\omega) + 1|^2} \Theta(\omega, T_B). \quad (39)$$

As can be seen, power absorbed by the particle has a distance dependence of $1/d^3$. Furthermore, the power absorbed is resonantly enhanced when the substrate supports surface waves ($|\epsilon_B(\omega) + 1| = 0$), or the particle has a localized resonance mode ($|\epsilon_p(\omega) + 2| = 0$). The origin of this resonantly enhanced power transfer in the near-field is the resonant enhancement of the EM-LDOS as discussed above. This approach can be refined further by considering non-local and retardation effects [83].

5.3. Heat transfer in non-standard geometries

A formalism for computing heat transfer for arbitrary objects has been derived for both in and out of equilibrium scenarios, based on the scattering properties of each individual object [95–97]. By introducing partial wave expansions, the resulting expressions for radiation, energy transfer, and forces can be transformed into traces of matrices that can be evaluated in any basis. The general applicability of this scattering matrix method has been verified by rederiving the heat transfer in the standard geometries of a plate, a sphere, and a cylinder near a planar interface [96,97].

5.4. Nano-scale heat transfer: experiment

Several experiments were performed to measure near-field radiative energy transfer. Anomalously large radiative heat transfer was already observed in the 1960s. Near-field heat transfer between two parallel chromium plates in vacuum separated by a gap of 50 μm to 1 mm was measured at room temperature, and enhanced heat transfer was observed [56]. Later a radiative heat transfer measurement at cryogenic temperatures between two copper plates at gaps below 1 μm was conducted and an increase of heat transfer with decreasing separation distance was shown [98].

More recently a measurement of the near-field heat transfer between a scanning tunneling microscope tip and gold or gallium nitride plates for a gap with distance of 100 to 1 nm was performed [99].

For a gap less than 10 nm, the measurements clearly showed near-field enhancement and the results agreed well with theory.

Large enhancements are predicted when the media support a surface-polariton excitation as discussed above. Near-field heat transfer measurements were performed near room temperature between two parallel quartz surfaces, which support surface phonon polaritons in the infrared region [88]. The measured near-field heat flux exceeded that between two blackbodies by $\sim 35\%$ when the vacuum gap was $1.6 \mu\text{m}$.

A sensitive technique for measuring near-field radiation between a silica micro-sphere and a quartz substrate using bimaterial atomic force microscope cantilevers as thermal sensors was developed [4,100] (Fig. 19a). Using this setup, heat transfer coefficients for a quartz surface at nano-scale gaps was measured to be 3 orders of magnitude larger than that of the blackbody radiation limit (solid line in Fig. 19b), indicating the enhancement due excitation of surface phonon polaritons between resonant materials.

5.5. Near-field heat transfer: applications

The possibility of achieving enhanced energy transfer in the near-field has attracted much attention. A number of applications have been developed such as nano-fabrication [101,102] and nanometer resolution thermometry [92,103,104]. The control of near-field heat transfer is also of great interest for applications such as energy conversion and radiative cooling [86,105–107].

One scheme proposed is to make use of the pseudomonochromatic nature of the energy transfer due to thermally excited surface waves on polar materials and the near-field effect for the purpose of improving the performance of thermal photovoltaic (PV) generators. With a thin layer of absorbing PV material close to a hot surface ($T \approx 1000 \text{ K}$), and by selecting the energy gap of the PV material to match the surface phonon polariton resonance frequency, one can improve the power absorption of PV material by three orders of magnitude at 20 nm separation compared to the solar isolation according to calculations, achieving 117 W/cm^2 [86]. However, only a single narrow band enhancement is achieved at the phonon polariton frequency.

More recently, metamaterials with hyperbolic dispersion have been proposed to engineer near-field thermal emission [106,108]. Metamaterials are a unique class of materials with either a negative electric permittivity, a negative magnetic permeability, or both. The power of metamaterials comes

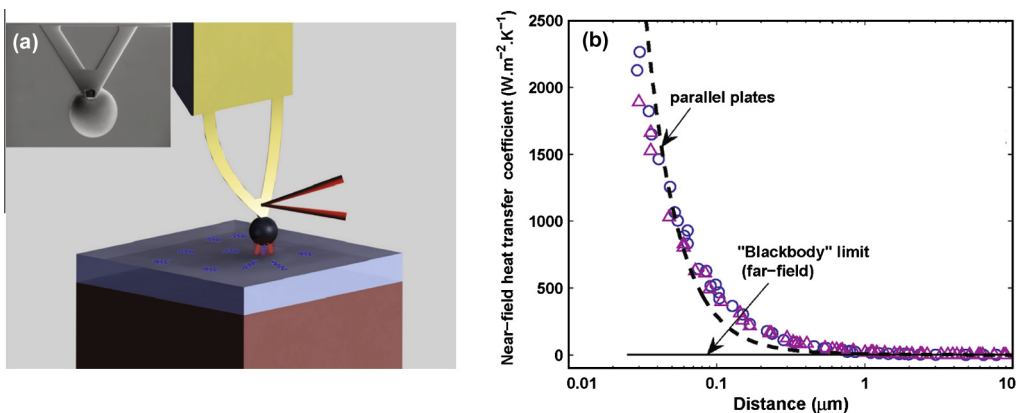


Fig. 19. (a) Measurement of near-field heat transfer between a SiO₂ sphere and a flat surface, based on a thermal sensor by measuring the deflection of a bimaterial AFM cantilever. Inset: SEM image of the SiO₂ sphere (100 μm in diameter) on the cantilever. (b) The measured thermal transfer coefficient shows a ~ 3 order of magnitude enhancement in the near-field regime for a 100 μm (blue circles) and a 50 μm (violet circles) diameter sphere. The flat line is the limit predicted by Planck's blackbody radiation law. The dashed line is the theoretical near-field heat transfer coefficients. Figure taken from Ref. [4]. (For interpretation of the references to color in this figure legend, the reader is referred to the web version of this article.)

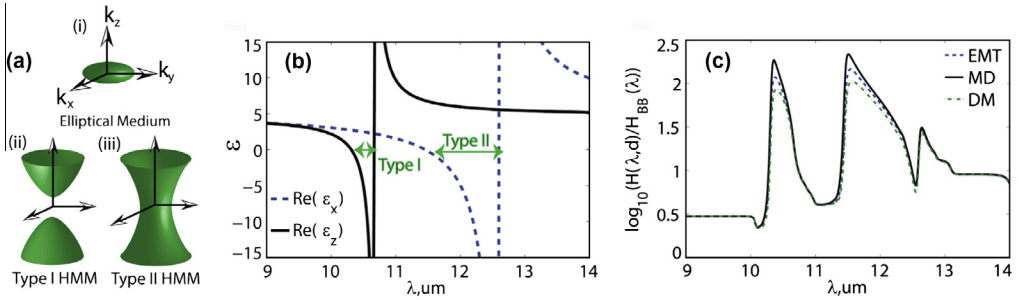


Fig. 20. (a) Iso-frequency surface in the k -space for three different types of metamaterials: (i) Ellipsoidal iso-frequency surface for effective anisotropic dielectric. (ii) Type I hyperbolic metamaterial (HMM) with only one negative component in the dielectric tensor. (iii) Type II HMM with two negative components. (b) Effective medium parameters of SiC-SiO₂ multilayers with layer thickness of 20 nm and SiC filling factor 0.3. (c) Heat transfer spectrum for two semi-infinite slabs, with one slab at 500 K and the other at 0 K. The fill fraction of SiC layer is 0.3 and the unit cell size is 20 nm. Black curve is the spectrum calculated with effective medium theory (EMT), while the blue and green curves are spectra accounting for surface effects. Blue curve represents the case when the topmost layer is metallic (MD); green curve for topmost dielectric layer (DM). Figure after Ref. [109]. (For interpretation of the references to color in this figure legend, the reader is referred to the web version of this article.)

from the ability to tune the permittivity and permeability to tailor optical properties that could not be readily found in nature. The iso-frequency surfaces of different metamaterials are illustrated in Fig. 20a as examples. In an isotropic medium, the dispersion relation $k^2/\epsilon = \omega^2/c^2$ defines a spherical iso-frequency surface in the k -space, thus placing an upper cut-off for the wavenumber so that high wavevector modes simply decay.

In contrast to this cut-off behavior, a strongly anisotropic metamaterial where the components of the dielectric permittivity tensor have opposite signs in two orthogonal directions can support bulk propagating waves with unbounded wavenumbers. These materials are known as *hyperbolic metamaterials* (HMMs) [109,110]. The propagating waves with large wavevector can be most clearly seen in the case of uniaxial anisotropy ($\epsilon_{zz} = \epsilon_{\parallel}$, $\epsilon_{xx} = \epsilon_{yy} = \epsilon_{\perp}$). Resorting to the iso-frequency surface of extraordinary waves in the effective uniaxial medium which follow $k_z^2/\epsilon_{\perp} + (k_x^2 + k_y^2)/\epsilon_{\parallel} = \omega^2/c^2$, one can see that the iso-frequency surface is hyperboloidal only when $\epsilon_{\perp} \cdot \epsilon_{\parallel} < 0$. One can effectively achieve a type I hyperbolic metamaterial with only one negative component in the dielectric tensor ($\epsilon_{xx} = \epsilon_{yy} > 0$, $\epsilon_{zz} < 0$), type II hyperbolic metamaterial with two negative components ($\epsilon_{xx} = \epsilon_{yy} < 0$, $\epsilon_{zz} > 0$), effective anisotropic dielectric ($\epsilon_{xx} = \epsilon_{yy} > 0$, $\epsilon_{zz} > 0$), or effective anisotropic metal ($\epsilon_{xx} = \epsilon_{yy} < 0$, $\epsilon_{zz} < 0$) [111]. Fig. 20b shows the effective medium dielectric function of a HMM consisting of a SiC/SiO₂ multilayer structure. By tuning the filling factor for SiC, one can tune the dielectric function of HMMs. The spectrum regions that support different hyperbolic dispersions are indicated with arrows.

One feature of the metamaterial approach compared to normal materials supporting surface phonon polaritons is broadband thermal emission beyond the blackbody limit in the near field [108,111]. The unique property of HMMs is the broad bandwidth in which the EM-LDOS is enhanced [106,112]. This broadband enhancement arises due to bulk high- k propagating waves in the metamaterial [110,113]. The role of the large enhancement in the density of states on the thermal emission is analyzed with fluctuational electrodynamics. With realistic material parameters, an enhancement of more than 200 is achieved over the whole Reststrahlen band for SiC [108] as shown in Fig. 20. Fig. 20c shows the heat transfer spectrum between two HMMs separated by a vacuum gap calculated by Eq. (35), combined with effective medium theory [106]. Super-Planckian thermal power transfer is reached in regions of hyperbolic dispersion, which agrees with previous analysis for material with surface polariton modes. The three peaks in the figure corresponds to two HMMs modes (the left and middle one) and one transverse optical phonon mode of SiC (the right one).

Besides enhanced energy transfer for heating, the enhanced near-field heat transfer can also be used for cooling, an effect recently demonstrated [107]. In Fig. 21a, a thermally isolated nano-structure is achieved with a suspended SiO₂ membrane in vacuum of 10^{-3} Pa, low enough that thermal

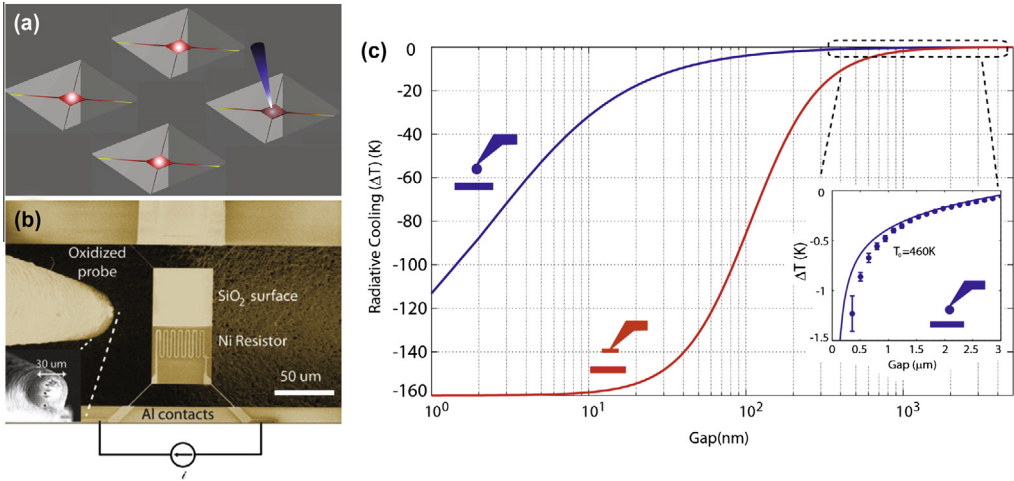


Fig. 21. Near-field cooling in sphere–plane interaction configuration. (a) Schematic of the experiment where one out of several isolated heat sources is cooled by radiative near-field coupling to a probe tip. (b) Top view SEM image of the suspended SiO₂ membrane with integrated resistor and the probe tip close to it. (c) Estimated temperature reduction of a 100 × 50 μm heat source, using either spherical or planar probes for dissipation. The spherical probe has a tip diameter of 30 μm. The heat source has a background conductance of 350 nW/K and is heated to an initial temperature of 460 K. Inset shows comparison of experimentally observed radiative cooling with the theoretical trend. Figure after Ref. [107].

conduction through air is negligible. Thermal isolation to the substrate is achieved by connecting the membrane to the substrate using thin spokes, resulting in low background conductance. The suspended SiO₂ membrane was heated with an integrated Ni resistor (Fig. 21b), and the calibrated temperature dependence of resistance is used to monitor the drop of membrane temperature when a 30 μm diameter SiO₂ probe particle was approached. A drop of 1.5 K was measured with gap size of 350 nm with initial temperature at 460 K.

Fig. 21c shows the theoretical prediction of temperature decrease of the SiO₂ membrane due to radiative cooling when another surface is brought closer, assuming either a spherical probe with 30 μm tip diameter (similar to experiment condition) or a parallel SiO₂ surface as a probe (red curve). In the simulations the membrane was heated to an initial temperature of 460 K, while the probe was at room temperature. The calculations are in good agreement with the experimental data (see Fig. 21c inset), and cooling by over 20 K should be achievable in the sub-50 nm regime using this configuration.

6. Thermal near-field optical forces

Radiative heat and associated energy transfer is closely related to momentum transfer or force. The force resulting from both zero temperature vacuum fluctuation and the finite temperature thermal fluctuation will be discussed here. We start with the vacuum induced force at zero temperature, then consider finite temperature effects. Finally the experimental confirmation of the thermal Casimir force is discussed.

6.1. Vacuum induced forces ($T = 0$ K)

An electromagnetic force exists between two neutral objects as a result of transient dipoles from quantum fluctuations originating from the finite vacuum ground state energy. This force is called the dispersive force, but is also known as the van der Waals, Casimir–Polder (of which the van der Waals force is a special case), or the Casimir force depending on the distance between objects and the dimensionality of the system [114]. The distinction between these nomenclatures is illustrated in Fig. 22.

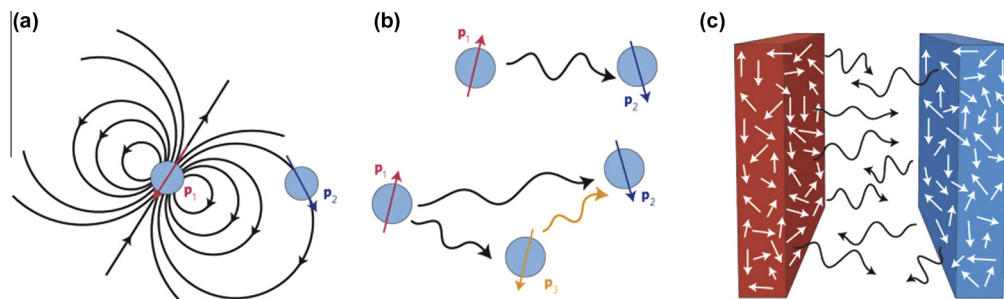


Fig. 22. Relationship between van der Waals (a), Casimir–Polder (b), and Casimir forces (c). Their common origin is the quantum (and thermal) fluctuations of dipoles. (a) A fluctuating dipole \mathbf{P}_1 induces a fluctuating electromagnetic dipole field, which in turn induces a fluctuating dipole \mathbf{P}_2 on a nearby particle, leading to van der Waals forces between the particles. (b) When the particle spacing is large, retardation/wave effects modify the interaction, leading to Casimir–Polder forces. When more than two particles interact, the non-additive field interactions lead to a breakdown of the pairwise force laws. (c) In situations consisting of macroscopic bodies, the interaction between the many fluctuating dipoles within the bodies leads to Casimir forces. Figure after Ref. [115].

At short distances (usually a few angstroms to a few nanometers), when the retardation effect due to the finite speed of light is negligible, the force between two atoms or molecules is called the van der Waals force (Fig. 22a). Its theory was developed by Fritz London when deriving the attractive force between atoms or molecules without a permanent electric dipole moment [116], and is therefore sometimes called the van der Waals–London force [114]. The force is typically in the range of few pN, and has a distance dependence $\propto 1/d^7$ for two atoms as an example. Before London’s calculation, the van der Waals attraction between polar molecules was recognized, but the origin of the experimentally observed nonzero van der Waals correction to the ideal gas law for non-polar gases such as helium was not clear. London explained that the origin of the attractive force between non-polar molecules or atoms is due to zero-point fluctuations in the charge distribution [117].

At large separation, on the order of, or larger than the characteristic wavelength of the material, retardation effects need to be accounted for. For metals the corresponding characteristic wavelength is c/ω_p , with ω_p the metal plasma frequency. Hendrik Casimir and Dirk Polder derived a general formula considering the retardation effect for the force between two atoms or between a plate and an atom. The force between two atoms or between a bulk object and an atom is thus often called the Casimir–Polder force (Fig. 22b) [6]. The general force formula between two neutral atoms has terms with different distance dependencies, and at the short distance limit, the van der Waals force expression $\propto 1/d^7$ is recovered. Consequently, the van der Waals force can be considered as the short distance limit of the Casimir–Polder force. Due to retardation, in the large distance limit the distance dependence of the force between two atoms is modified to $\propto 1/d^8$ [6].

Shortly thereafter, Casimir studied the vacuum induced force between two perfect conducting plates, and the resulting force has been named the Casimir force (Fig. 22c) [7]. The difference from the Casimir–Polder force is that the interaction between many particles is generally non-additive. When these multiple scattering effects are combined under consideration of wave retardation, one retrieves the Casimir force.

For comparison we list some typical force values here. Brownian motion exerts forces on particles in the low pN range, molecular motors create forces in the sub 10-pN range, antigen–antibody interactions are 50–300 pN, and several nN will break a C–C bond [118].

6.1.1. Theory of the Casimir force

In 1948 Casimir calculated the force between two infinitely large parallel ideal metal walls due to the vacuum fluctuation at zero temperature [6]. The roots of this effect date back to the introduction by Planck in 1911 of the energy quanta [119]. In quantum mechanics a harmonic oscillator has energy levels $E_n = \hbar\omega(n + 1/2)$, where $n = 0, 1, \dots$ and ω is the harmonic oscillation frequency. It is the role of the ground state energy $E_0 = \frac{1}{2}\hbar\omega$ that distinguishes the Casimir force from classical electrodynamics.

According to quantum theory, the electromagnetic field confined between two perfect conducting plates, separated by distance d , are discrete modes with frequency $\omega_n = n\pi c/d$. The sum over the zero-point energy for all the infinite number of modes inside the two plates is given by

$$E = \sum_n \frac{1}{2} \hbar \omega_n, \quad (40)$$

with E becoming infinite. It was Casimir who obtained a finite force expression from the infinite sum. The Casimir force is the difference between the vacuum electromagnetic energy for infinite plate separation ($d = \infty$) and finite plate separation d . The result of the force per unit area is

$$F_c = -\frac{\hbar c \pi^2}{240 d^4} = -\frac{1.3 \times 10^{-27} \text{ N/m}^2}{d^4}. \quad (41)$$

This attractive Casimir force due to quantum fluctuation has been studied extensively with high accuracy under different geometries [120–126]. We will discuss some of the experiments in the next section.

The Casimir force in its details depends both on geometry and material properties. The geometric dependence through boundary conditions has been studied widely [127–132]. One geometry commonly adopted in experiments to avoid the difficulty of aligning two parallel flat planes is one flat plate and one large sphere (sphere–plane geometry). For ideal metals and separation between sphere and plane d much smaller than the sphere radius R , the zero-temperature Casimir force is [133]

$$F_c = -\frac{\hbar c \pi^3 R}{360 d^3}, \quad (42)$$

which has a different distance dependence than the case of two parallel plate geometry. Calculations of Casimir forces in more complex geometries have been hampered by the lack of theoretical tools capable of describing arbitrary geometries, and can sometimes yield contradictory results [134,135], yet progress has been made with the development of refined theory and numerical methods [95–97,129,136,137].

The Casimir force can also be modified by varying the dielectric function of the media $\epsilon(\omega) = \epsilon'(\omega) + i\epsilon''(\omega)$ [114,138–140]. The theory of the Casimir force for real material was developed by Lifshitz [8]. It is based on the calculation of the Maxwell's stress tensor by considering the fluctuation of electromagnetic fields using the fluctuation-dissipation theorem, and the result is expressed in terms of $\epsilon(\omega)$ of the material of the plate.

At zero temperature, the force between two planar half-spaces made from identical materials can be expressed as an integration over frequency [8]:

$$F = \int_0^\infty \frac{d\omega}{2\pi} \int_0^\infty \frac{du}{2\pi} F(u, \omega), \quad (43)$$

$$\text{with } F(u, \omega) = \frac{2\hbar\omega^3 u}{c^3} \text{Im} \left(v \sum_{q=s,p} \frac{(r^q)^2(u, \omega) e^{-2\omega v d}}{1 - (r^q)^2(u, \omega) e^{-2\omega v d/c}} \right), \quad (44)$$

where $v = (u^2 - 1)^{1/2}$ ($\text{Im}v \leq 0$), and r^q is the Fresnel reflection coefficient for a plane wave with polarization q , and $u = k_{\parallel}/k$, with k_{\parallel} parallel with respect to the interface. In connection to the near-field EM-LDOS, the contribution of surface polariton modes to the Casimir force has been discussed, and can dramatically modify the force [141–144].

A repulsive Casimir force was predicted theoretically for certain material properties [134,139,141,145,146]. This prediction can qualitatively be understood from inspecting the term inside Eq. (44),

$$\sum_{q=s,p} \frac{(r^q)^2(u, \omega) e^{-2\omega v d}}{1 - (r^q)^2(u, \omega) e^{-2\omega v d/c}}. \quad (45)$$

By tuning the reflection coefficients $(r^q)^2(u, \omega)$ through different material resonances, the force can be modified. As an example, repulsive forces are predicted to arise in materials with high magnetic per-

meability [134,135,140], though the experimental verification with vacuum as interaction medium is still outstanding. However, replacing vacuum with a real medium, a repulsive Casimir force could be demonstrated [147,148].

6.1.2. Casimir force: experiment

Comparison between experiment and theory of the Casimir force is summarized in Refs. [3,114,149,150], including the effects of surface roughness, oxide coating, surface contamination, and uncertainty in the optical properties of the material. These effects can dramatically change the magnitude of the force, and need to be properly accounted for in order to calculate the force to better than 10% for two plates separation distances less than 1 μm . 5% experiment precision was achieved by Lamoreaux in 1997 using a torsion balance to measure the Casimir force between a gold-coated spherical lens and a plane [120], followed by other precision Casimir measurements [121,122,151,149,152]. A high precision Casimir force measurement with two parallel plates has also been performed [126].

A repulsive force between a Cs atom at resonance of the $6D_{3/2} \rightarrow 7P_{1/2}$ transition and a sapphire plate was observed [153]. But the corresponding repulsive Casimir forces between macroscopic objects was much more difficult to measure. This repulsive effect was recently observed using a gold coated polystyrene sphere and a silica plate separated by a bromobenzene liquid ($\epsilon_{\text{gold}} > \epsilon_{\text{bromobenzene}} > \epsilon_{\text{silica}}$) [148].

Fig. 23a shows the schematic setup of the repulsive Casimir force experiment. It consists of a large plane and a 39.8 mm diameter polystyrene sphere coated with a 100 nm thick gold film, which is attached to a cantilever and mounted on an atomic force microscope with a fluid-filled cell. Inequality ($\epsilon_1 > \epsilon_3 > \epsilon_2$) over a large frequency range is needed to achieve a net repulsive force. One set of materials (solid-liquid-solid) that satisfies this inequality is gold, bromobenzene and silica (Fig. 23b). The measured force curve is shown in Fig. 23c. The blue curve corresponds to the repulsive force between the gold sphere and the silica plate. A control experiment is done by replacing the silica plate with a gold plate, and an attractive force was observed as expected (yellow curve in Fig. 23c).

The modification of the Casimir force through the radiation induced change in the carrier density in the media has been observed between a gold coated sphere and a single-crystal Si membrane [154,155]. The result suggests a modification of the Casimir force due to thermally induced changes of the material properties is feasible, and by engineering material properties and geometry, i.e., using hole arrays or other nano-structured metallic surfaces, it may be possible to realize an enhancement of the force or even a sign change [138,141,144,156].

6.2. Thermally induced force (finite temperature)

At finite temperature T , there are additional thermal fluctuations generating thermal photons at excited states that shift the average photon energy to $(n(\omega) + 1/2)\hbar\omega$, with the thermal photon

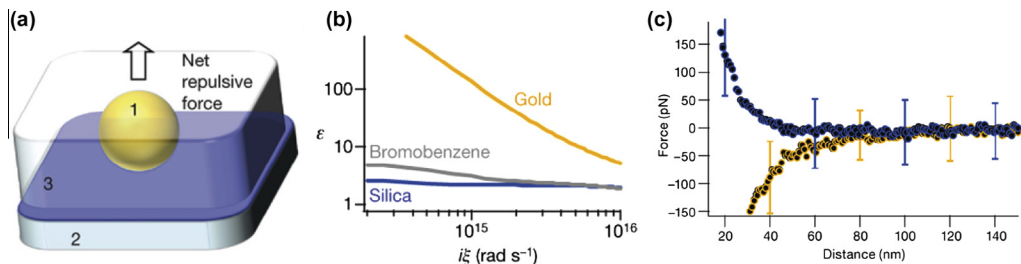


Fig. 23. Repulsive quantum electrodynamic forces can exist for two materials separated by a fluid. (a) The interaction between material 1 and material 2 immersed in a fluid (material 3) is repulsive when material dielectric function satisfy $\epsilon_1 > \epsilon_3 > \epsilon_2$. (b) The optical properties of gold, bromobenzene and silica are such that $\epsilon_{\text{gold}} > \epsilon_{\text{bromobenzene}} > \epsilon_{\text{silica}}$ and lead to a repulsive force between the gold and silica surfaces. (c) Blue (yellow) circles represent the force between a gold sphere and a silica (gold) plate in bromobenzene. Figure after Ref. [148]. (For interpretation of the references to color in this figure legend, the reader is referred to the web version of this article.)

occupation number $n(\omega) = 1/(e^{\hbar\omega/kT} - 1)$. The correction of the Casimir force due to these thermal photons is called thermal Casimir effect.

The finite temperature force formula for two parallel ideal metal plates can be obtained by replacing $\frac{1}{2}\hbar\omega$ in the energy summation with the mean photon energy $(n(\omega) + 1/2)\hbar\omega$, resulting in [157]

$$F_c(T) = -\frac{\hbar c\pi^2}{240d^4} \left[1 - \frac{240}{\pi} \frac{k_B T d}{\hbar c} e^{-\pi\hbar c/k_B T d} + \frac{48}{9} \left(\frac{k_B T d}{\hbar c} \right)^4 \right]. \tag{46}$$

Compared to the zero temperature quantum Casimir force, the thermal effect is small at room temperature and short distances, thus difficult to measure experimentally. But the thermal effect would dominate the Casimir force at long distances.

The geometry that has been adopted in experiment is a sphere–plane geometry. In this geometry, the thermal Casimir force due to finite temperature alone has been calculated using a Drude model $\epsilon(\omega) = 1 - \omega_p^2/(\omega(\omega + i\gamma))$ resulting in [158,159]:

$$F_c^{(T)} \approx \frac{1.202}{8} \frac{Rk_B T}{d^2}, \tag{47}$$

with R the sphere radius and d the separation. This thermal Casimir force dominates over the purely quantum ($T = 0$ K) Casimir force at large distances (which scales as $\sim 1/d^3$ in Eq. (42)) [151,160–163].

Thermal fluctuations would also change the force on a point-like particle in front of a plate, which is the thermal Casimir–Polder force. Generally the force felt by a point-like particle near the surface of a substrate due to quantum or thermal fluctuation can be modeled as follows [156,164,165],

$$F_z(r) = \sum_{i=x,y,z} \langle \vec{d}_i(t) \partial_z E_i(r, t) \rangle, \tag{48}$$

where $\vec{d}(t)$ is the induced dipole moment of the particle by the fluctuating electric field $E(r, t)$ at the particle’s position

$$\vec{d}(\omega) = \epsilon_0 \alpha(\omega) E(r, \omega), \tag{49}$$

with $\alpha(\omega)$ the spherical particle polarizability $\alpha(\omega) = 4\pi a^3(\epsilon_p(\omega) - 1)/(\epsilon_p(\omega) + 2)$.

By rewriting $E(\omega, r)$ in terms of the Green’s dyadic functions (Eq. (15)) and applying the fluctuation dissipation theorem (Eq. (16)) one obtains,

$$F_z(r) = F_{\text{vac}}(z) + F_{\text{th}}(z), \tag{50}$$

with

$$F_{\text{vac}}(z) = \frac{\hbar\epsilon_0}{\pi} \text{Im} \left(\int_0^\infty d\omega \alpha(\omega) \nabla_z \vec{G}_{ii}^E(\omega, z, z) \right), \tag{51}$$

and

$$F_{\text{th}}(z) = \frac{2\epsilon_0}{\pi} \int_0^\infty d\omega \frac{\Theta(\omega, T)}{\omega} \text{Im} \epsilon_1(\omega) \text{Re} \left[\alpha(\omega) \nabla \vec{S}_{ii}^*(\omega, z, z) \right] \tag{52}$$

where

$$S_{ij}(\omega, r, r') = \int d^3x G_{ik}^E(\omega, r, x) G_{jk}^{E*}(\omega, r', x). \tag{53}$$

The F_{vac} represents the vacuum induced force and F_{th} is due to thermal fluctuation.

The thermal induced force has a different distance dependence than the vacuum induced counterpart. At distances larger than the thermal photon wavelength $\lambda_T = \hbar c/k_B T$ ($\sim 7.6 \mu\text{m}$ at room temperature), the force between an atom and a surface decays as $1/d^4$ at thermal equilibrium (in contrast to $1/d^5$ at zero temperature) [164].

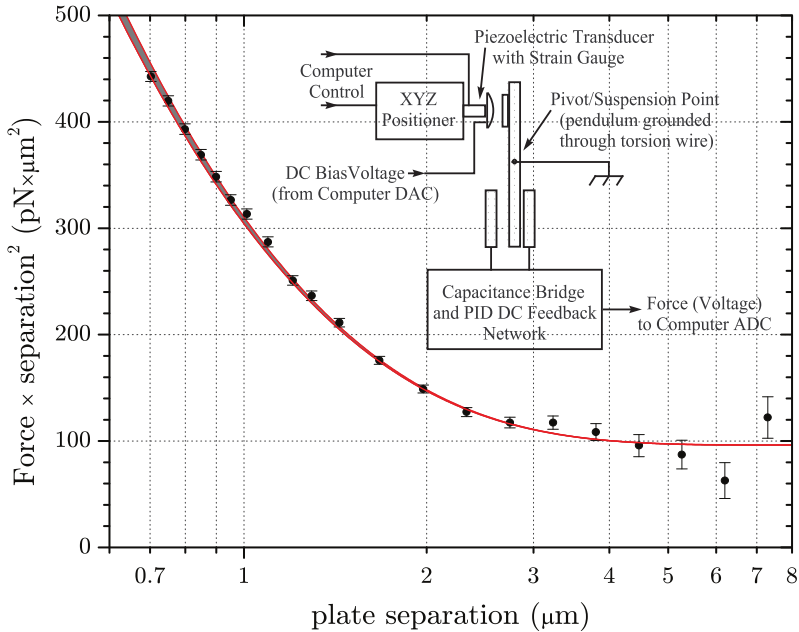


Fig. 24. Measured thermal Casimir force corrected for electrostatic force, in comparison with theory at $T = 300$ K (red lines). The gray band represents theoretical uncertainty in the Casimir force calculation from the measured material dielectric function used as input parameter. The data are plotted as $F \times d^2$ (Eq. (47)), so that the thermal Casimir force corresponds to an offset of $97 \text{ pN} \times \mu\text{m}^2$, which dominates the force at large plate separations ($\gtrsim 3 \mu\text{m}$). In this region the Casimir force is largely independent of the material properties of the plates. The inset shows the schematic of the torsion pendulum experimental apparatus. The torsion pendulum is suspended inside a vacuum chamber (pressure $\sim 10^{-4}$ Pa) by a tungsten wire. Figure after Ref. [159]. (For interpretation of the references to color in this figure legend, the reader is referred to the web version of this article.)

When particle radius a is comparable to the separation distance d , multipole effects should be taken into account, for example when $d/a < 2$ the quadrupole-quadrupole interactions become dominant [166].

6.2.1. Thermal Casimir force: experiment

Experiments with a Bose-Einstein condensate in front of a fused-silica surface seemed to observe the modified distance dependence of the Casimir–Polder force due to finite temperature, and the measured force gradient increased by a factor of 3 at ~ 600 K compared to the room temperature value [167].

The macroscopic thermal Casimir force (in the 1–10 pN range) was also observed recently under a sphere–plane geometry in the separation range of 0.7 to $7 \mu\text{m}$ [168]. Fig. 24 (inset) shows the schematic of the suspended torsion pendulum based measurement device. The force is measured between a gold-coated spherical surface (radius 15.6 cm) and a gold-coated slab. The device is at room temperature ($T = 300 \pm 1$ K) and in high vacuum of $\sim 10^{-4}$ Pa. Fig. 24 shows the distance dependence of the force between two gold plates, plotted as $F \times d^2$ corresponding to Eq. (47). The experimental result agrees with calculation from Lifshitz theory (red curve), with a plateau at distances of $\gtrsim 3 \mu\text{m}$ showing the dominant role of the thermal Casimir force at long distances. The plateau at long distance is the evidence of a $1/d^2$ dependence of the force rather than $1/d^3$ as in the case of vacuum Casimir force at separations greater than $3 \mu\text{m}$.

This experimental result raises interesting questions, such as how much the force can be modified by selectively enhancing EM-LDOS at different frequencies through engineered nano heated sources.

7. Outlook

Thermal near-field optics is a field still in its infancy. The discussions above show that many open questions remain regarding the fundamental nature of the thermal near-field and its spatial, spectral, and coherence properties. The results presented suggest that by suitable control of the material properties, resonances, and geometries, including precise spatial control, many yet unexplored opportunities exist for spectroscopy, the control of heat transfer, and optical forces.

The spectroscopic characterization of the enhanced electromagnetic near-field spectral energy densities connects the previously well-defined regime of broadband far-field thermal radiation to the prediction of intrinsic and extrinsic thermal near-field resonances and their wavevector distribution. Thermal infrared near-field spectroscopy, a new scattering-type scanning near-field optical microscopy technique, has opened the door for these spectral and spatial characterizations of the fundamental thermal near-field properties. It can either serve as a sensitive probe of the fundamental electromagnetic local density of state (EM-LDOS) properties of the sample when the tip acts as a minimally invasive Rayleigh point scatterer. It can also serve as a tool for surface infrared vibrational nano-spectroscopy and -imaging. Here, the thermally driven vibrational modes provide their own intrinsic light source, i.e., making the sample its own light source, for broadband chemical nano-spectroscopy. Its sensitivity can be improved utilizing IR optical antenna modes of specially engineered tips, and is expected to compete favorably with laser-based techniques.

The spatial coherence and enhanced transport properties associated with the thermal near-field at dimensions on the order of the peak emission wavelength, should allow for thermally excited infrared antenna structures, directional thermal emitters, and metamaterials designed for enhanced thermal emission or absorption. Similarly, a new unifying discussion of the different mechanisms of optical forces, driven either by quantum or thermal fluctuations is now possible, combining van der Waals, Casimir, and Casimir–Polder forces, and their extension to resonant and finite temperature interactions and control. In addition to new fundamental physics, the door is open for many practical applications, e.g., tailoring heat management in microelectronic and thermophotovoltaic devices, optical antenna resonant control and switching of optical forces, enhanced IR and thermal sensing, and compact chemical nano-imaging and -spectroscopy instrumentation. Despite being evanescent in nature and thus invisible to most conventional techniques we predict a rich future for the new field of thermal near-field optics.

Acknowledgments

We gratefully acknowledge valuable discussions with Jean-Jacques Greffet, Prashant Nagpal, Reddy Pramod, and Yannick De Wilde. We thank Robert Olmon for his help in thermal tip modification and s-SNOM instrument development. We also thank Eric Muller, William Lewis and Samuel Berweger for help with new thermal near-field spectroscopy experiments. We are indebted to Kevin Kjoller and the team from Anasys Instruments for continuous support. Funding was provided by in part by DoE:STTR Grant (DE-FG02-08ER86338).

References

- [1] Z. Zhang, *Nano/Microscale Heat Transfer*, McGraw Hill, 2007.
- [2] K. Joulain, J.-P. Mulet, F. Marquier, R. Carminati, J.-J. Greffet, Surface electromagnetic waves thermally excited: radiative heat transfer, coherence properties and Casimir forces revisited in the near field, *Surf. Sci. Rep.* 57 (3–4) (2005) 59–112.
- [3] A. Volokitin, B. Persson, Near-field radiative heat transfer and noncontact friction, *Rev. Mod. Phys.* 79 (4) (2007) 1291–1329.
- [4] S. Shen, A. Narayanaswamy, G. Chen, Surface phonon polaritons mediated energy transfer between nanoscale gaps, *Nano Lett.* 9 (8) (2009) 2909–2913.
- [5] S. Basu, Z.M. Zhang, C.J. Fu, Review of near-field thermal radiation and its application to energy conversion, *Int. J. Energy Res.* 33 (13) (2009) 1203–1232.
- [6] H.B.G. Casimir, D. Polder, The influence of retardation on the London–van der Waals forces, *Phys. Rev.* 73 (4) (1948) 360–372.
- [7] H.B.G. Casimir, On the attraction between two perfectly conducting plates, *Proc. Kon. Nederland. Akad. Wetensch.* B51 (1948) 793.
- [8] E.M. Lifshitz, The theory of molecular attractive forces between solids, *J. Exp. Theor. Phys. USSR* 29 (1955) 94–110.

- [9] F. Herschel, Philos. Trans. R. Soc. Lond. 90 (1800) 437.
- [10] G. Kirchhoff, Über den Zusammenhang zwischen Emission und Absorption von Licht und Wärme, Monatsber. Preuss. Akad. (1859) 783–787.
- [11] M. Planck, Zur Theorie des Gesetzes der Energieverteilung im Normalspektrum, Verh. Phys. Ges. 2 (1900) 237–245.
- [12] I. Müller, A History of Thermodynamics, Springer, 2007.
- [13] J. Fraunhofer, Bestimmung des Brechungs- und des Farben-Zerstreuungs - Vermögens verschiedener Glasarten, in Bezug auf die Vervollkommnung achromatischer Fernröhre, Denkschriften der Königlichen Akademie der Wissenschaften zu München, 5 (1872) 193–226.
- [14] G. Kirchhoff, Über das Verhältnis zwischen dem Emissionsvermögen und dem Absorptionsvermögen der Körper für Wärme und Licht, Ann. Phys. Chem. 109 (1860) 275–301.
- [15] J. Mehra, H. Rechenberg, The Historical Development of Quantum Theory, Springer, 2000.
- [16] J. Stefan, Über die Beziehung zwischen der Wärmestrahlung und der Temperatur, Sitzber. Akad. Wiss. Wien. 79 (1879) 391–428.
- [17] J. Crepeau, A brief history of the T^4 radiation law, 2009 ASME Summer Heat Transfer Conference, 2009.
- [18] J. Tyndall, On Radiation, Appleton and Co., 1865.
- [19] L. Boltzmann, Ableitung des Stefan'schen Gesetzes, betreffend die Abhängigkeit der Wärmestrahlung von der Temperatur aus der elektromagnetischen Lichttheorie, Ann. Phys. 258 (1884) 291–294.
- [20] O. Lummer, E. Pringsheim, Die Vertheilung der Energie im Spektrum des Schwarzen Körpers, Verh. Phys. Ges. 1 (1899) 23–41.
- [21] Otto Lummer - Leben und Wirken, 2009. <http://www.otto-lummer.de/index.html>.
- [22] W. Wien, O. Lummer, Methode zur Prüfung des Strahlungsgesetzes absolut schwarzer Körper, Ann. Phys. 292 (1897) 451–456.
- [23] O. Lummer, E. Pringsheim, Die Strahlung eines "schwarzen Körpers zwischen 100 und 1300°C, Ann. Phys. 299 (1897) 395–410.
- [24] O. Lummer, E. Pringsheim, Über die Strahlung des schwarzen Körpers für lange Wellen, Verh. Dt. Phys. Ges. 2 (1900) 163–180.
- [25] O. Lummer, E. Pringsheim, Die Verteilung der im Spektrum des schwarzen Körpers und des blanken Platins, Verh. Dt. Phys. Ges. 1 (1899) 215–235.
- [26] W. Wien, Eine neue Beziehung der Strahlung schwarzer Körper zum zweiten Hauptsatz der Wärmetheorie, Sitzungsber. Preuss. Akad. (1893) 55–62.
- [27] W. Wien, Über die Energieverteilung im Emissionsspektrum eines schwarzen Körpers, Ann. Phys. 299 (1896) 662–669.
- [28] J.H. Jeans, J.W.S. Rayleigh, The dynamical theory of gases and of radiation, Nature 72 (1905) 54.
- [29] C. Gearhart, Planck, the quantum, and the historians, Phys. Perspect. 4 (2002) 170–215.
- [30] E. Chaisson, S. McMillan, Astronomy Today, Prentice Hall, 1999.
- [31] S. Chiang, R.G. Tobin, P.L. Richards, Vibrational spectroscopy of chemisorbed molecules by infrared emission, J. Vac. Sci. Technol. A 2 (2) (1984) 1069–1074.
- [32] D. Allara, D. Teicher, J. Durana, Fourier transform infrared emission spectrum of a molecular monolayer at 300 K, Chem. Phys. Lett. 84 (1) (1981) 20–24.
- [33] E.H. Korte, A. Röseler, Infrared Reststrahlen revisited: commonly disregarded optical details related to $n < 1$, Anal. Bioanal. Chem. 382 (2005) 1987–1992.
- [34] C. Henkel, K. Joulain, R. Carminati, J. Greffet, Spatial coherence of thermal near fields, Opt. Commun. 186 (2000) 57–67.
- [35] J.-P. Mulet, K. Joulain, R. Carminati, J.-J. Greffet, Nanoscale radiative heat transfer between a small particle and a plane surface, Appl. Phys. Lett. 78 (19) (2001) 2931.
- [36] K. Joulain, R. Carminati, J.-P. Mulet, J.-J. Greffet, Definition and measurement of the local density of electromagnetic states close to an interface, Phys. Rev. B 68 (24) (2003) 245405.
- [37] J.E. Sipe, New Green-function formalism for surface optics, J. Opt. Soc. Am. B 4 (4) (1987) 481.
- [38] R. Carminati, J.-J. Greffet, Near-field effects in spatial coherence of thermal sources, Phys. Rev. Letters 82 (8) (1999) 1660–1663.
- [39] S. Volz (Ed.), Microscale and Nanoscale Heat Transfer, Springer, 2007.
- [40] H.O. McMahon, Thermal radiation from partially transparent reflecting bodies, J. Opt. Soc. Am. 40 (6) (1950) 376–378.
- [41] M.B. Raschke, S. Berweger, J.M. Atkin, Ultrafast and nonlinear plasmon dynamics in *Plasmonics: Theory and Applications* (T.V. Shahbazyan, M.I. Stockman (Eds.)), Springer, 2014.
- [42] E. Palik (Ed.), Handbook of Optical Constants of Solids, vol. 1, Academic Press, 1985.
- [43] C.Y. Liang, S. Krimm, Infrared spectra of high polymers. III. Polytetrafluoroethylene and polychlorotrifluoroethylene, J. Chem. Phys. 25 (3) (1956) 563–571.
- [44] R.E. Moynihan, The molecular structure of perfluorocarbon polymers. Infrared studies on polytetrafluoroethylene, J. Am. Chem. Soc. 81 (5) (1959) 1045–1050.
- [45] W.G. Spitzer, D.A. Kleinman, Infrared lattice bands of quartz, Phys. Rev. 121 (5) (1961) 1324–1335.
- [46] J.F. Scott, S.P.S. Porto, Longitudinal and transverse optical lattice vibrations in quartz, Phys. Rev. 161 (3) (1967) 903–910.
- [47] A. Jones, M. Raschke, Thermal infrared near-field spectroscopy, Nano Lett. 12 (3) (2012) 1475–1481.
- [48] J.-J. Greffet, R. Carminati, K. Joulain, J.-P. Mulet, S. Mainguy, Y. Chen, Coherent emission of light by thermal sources, Nature 416 (6876) (2002) 61–64.
- [49] E. Wolf, Coherence and radiometry, J. Opt. Soc. Am. 68 (1) (1978) 6–17.
- [50] C. Arnold, F. Marquier, M. Garin, F. Pardo, S. Collin, N. Bardou, J.-L. Pelouard, J.-J. Greffet, Coherent thermal infrared emission by two-dimensional silicon carbide gratings, Phys. Rev. B 86 (2012) 035316.
- [51] P.J. Hesketh, J.N. Zemel, B. Gebhart, Polarized spectral emittance from periodic micromachined surfaces. I. Doped silicon: the normal direction, Phys. Rev. B 37 (1988) 10795–10802.
- [52] P.J. Hesketh, J.N. Zemel, B. Gebhart, Polarized spectral emittance from periodic micromachined surfaces. II. Doped silicon: angular variation, Phys. Rev. B 37 (1988) 10803–10813.

- [53] J. Le Gall, M. Olivier, J.-J. Greffet, Experimental and theoretical study of reflection and coherent thermal emission by a sic grating supporting a surface-phonon polariton, *Phys. Rev. B* 55 (1997) 10105–10114.
- [54] A. Shchegrov, K. Joulain, R. Carminati, J. Greffet, Near-field spectral effects due to electromagnetic surface excitations, *Phys. Rev. Lett.* 85 (7) (2000) 1548–1551.
- [55] J.B. Pendry, Radiative exchange of heat between nanostructures, *J. Phys. Condens. Matter* 11 (35) (1999) 6621–6633.
- [56] C. Hargreaves, Anomalous radiative transfer between closely-spaced bodies, *Phys. Lett. A* 30 (9) (1969) 491–492.
- [57] F. Gervais, B. Piriou, Temperature dependence of transverse and longitudinal optic modes in the α and β phases of quartz, *Phys. Rev. B* 11 (10) (1975) 3944–3950.
- [58] E. Rousseau, A. Siria, G. Jourdan, S. Volz, F. Comin, J. Chevrier, J.-J. Greffet, Radiative heat transfer at the nanoscale, *Nat. Photon.* 3 (9) (2009) 514–517.
- [59] Y. Kajihara, K. Kosaka, S. Komiyama, A sensitive near-field microscope for thermal radiation, *Rev. Sci. Instrum.* 81 (3) (2010) 033706.
- [60] Y.D. Wilde, F. Formanek, R. Carminati, B. Gralak, P. Lemoine, K. Joulain, J. Mulet, Y. Chen, J. Greffet, Thermal radiation scanning tunneling microscopy, *Nature* 444 (2006) 740–743.
- [61] A. Kittel, U.F. Wischnath, J. Welker, O. Huth, F. Ruting, S.-A. Biehs, Near-field thermal imaging of nanostructured surfaces, *Appl. Phys. Lett.* 93 (19) (2008) 193109.
- [62] M.B. Raschke, C. Lienau, Apertureless near-field optical microscopy: tip-sample coupling in elastic light scattering, *Appl. Phys. Lett.* 83 (24) (2003) 5089–5091.
- [63] R. Hillenbrand, F. Keilmann, Near-field microscopy by elastic scattering from a tip, *Phil. Trans. R. Soc. Lond. A* 362 (2004) 787–805.
- [64] P.-O. Chapuis, J.-J. Greffet, K. Joulain, S. Volz, Heat transfer between a nano-tip and a surface, *Nanotechnology* 17 (12) (2006) 2978–2981.
- [65] N. Behr, M.B. Raschke, Optical antenna properties of scanning probe tips: plasmonic light scattering, tip-sample coupling, and near-field enhancement, *J. Phys. Chem. C* 112 (10) (2008) 3766–3773.
- [66] R.L. Olmon, M. Rang, P.M. Krenz, B.A. Lail, L.V. Saraf, G.D. Boreman, M.B. Raschke, Determination of electric-field, magnetic-field, and electric-current distributions of infrared optical antennas: a near-field optical vector network analyzer, *Phys. Rev. Lett.* 105 (16) (2010) 167403.
- [67] C. Bohren, D. Huffman, *Absorption and Scattering of Light by Small Particles*, Wiley & Sons, 1983.
- [68] R. Hillenbrand, T. Taubner, F. Keilmann, Phonon-enhanced light-matter interaction at the nanometre scale, *Nature* 418 (2002) 159.
- [69] A. Cvitkovic, N. Ocelic, R. Hillenbrand, Analytical model for quantitative prediction of material contrasts in scattering-type near-field optical microscopy, *Opt. Express* 15 (14) (2007) 8550–8565.
- [70] J.A. Schuller, T. Taubner, M.L. Brongersma, Optical antenna thermal emitters, *Nat. Photon.* 3 (11) (2009) 658–661.
- [71] C.R. Otey, W.T. Lau, S. Fan, Thermal rectification through vacuum, *Phys. Rev. Lett.* 104 (15) (2010) 154301.
- [72] A.K. Hafeli, E. Rephaeli, S. Fan, D.G. Cahill, T.E. Tiwald, Temperature dependence of surface phonon polaritons from a quartz grating, *J. Appl. Phys.* 110 (4) (2011) 043517 (5pp).
- [73] A. Abuty, K. Joulain, P.-O. Chapuis, J. Greffet, Y. de Wilde, Blackbody spectrum revised in the near-field, *Phys. Rev. Lett.* 110 (2013) 146103.
- [74] B.T. O’Callahan, W.E. Lewis, Andrew C. Jones, M.B. Raschke, Spectral frustration and coherence in thermal near-field spectroscopy, in preparation.
- [75] R.L. Olmon, M.B. Raschke, Antennal load interactions at optical frequencies: impedance matching to quantum systems, *Nanotechnology* 23 (44) (2012) 444001.
- [76] X.G. Xu, M.B. Raschke, Infrared near-field vibrational dynamics and antenna-assisted decoherence on the nanoscale, *Nano Lett.* 13 (2013) 1588.
- [77] H.A. Bechtel, M.C. Martin, P. Lerch, Improved spatial resolution for reflection mode infrared microscopy, *Rev. Sci. Instrum.* 80 (12) (2009) 126106.
- [78] M.B. Raschke, L. Molina, T. Elsaesser, D.H. Kim, W. Knoll, K. Hinrichs, Apertureless near-field vibrational imaging of block-copolymer nanostructures with ultrahigh spatial resolution, *ChemPhysChem* 6 (2005) 2197.
- [79] F. Huth, M. Schnell, J. Wittborn, N. Ocelic, R. Hillenbrand, Infrared-spectroscopic nanoimaging with a thermal source, *Nat. Mater.* 10 (5) (2011) 352–356.
- [80] S.M. Rytov, *Theory of Electrical Fluctuation and Thermal Radiation*, Academy of Science of USSR Publishing, Moscow, 1953.
- [81] D. Polder, M. Van Hove, Theory of radiative heat transfer between closely spaced bodies, *Phys. Rev. B* 4 (10) (1971) 3303–3314.
- [82] J. Loomis, H. Maris, Theory of heat transfer by evanescent electromagnetic waves, *Phys. Rev. B* 50 (24) (1994) 18517–18524.
- [83] A. Volokitin, B. Persson, Radiative heat transfer between nanostructures, *Phys. Rev. B* 63 (20) (2001) 205404.
- [84] J.-P. Mulet, K. Joulain, R. Carminati, J.-J. Greffet, Enhanced radiative heat transfer at nanometric distances, *Microscale Thermophys. Eng.* 6 (3) (2002) 209–222.
- [85] C. Fu, Z. Zhang, Nanoscale radiation heat transfer for silicon at different doping levels, *Int. J. Heat Mass Transfer* 49 (9–10) (2006) 1703–1718.
- [86] A. Narayanaswamy, G. Chen, Surface modes for near field thermophotovoltaics, *Appl. Phys. Lett.* 82 (20) (2003) 3544.
- [87] A. Volokitin, B. Persson, Resonant photon tunneling enhancement of the radiative heat transfer, *Phys. Rev. B* 69 (4) (2004) 045417.
- [88] L. Hu, A. Narayanaswamy, X. Chen, G. Chen, Near-field thermal radiation between two closely spaced glass plates exceeding Planck’s blackbody radiation law, *Appl. Phys. Lett.* 92 (13) (2008) 133106.
- [89] M. Francoeur, M.P. Menguc, R. Vaillon, Near-field radiative heat transfer enhancement via surface phonon polaritons coupling in thin films, *Appl. Phys. Lett.* 93 (4) (2008) 043109.
- [90] G. Agarwal, Quantum electrodynamics in the presence of dielectrics and conductors. I. Electromagnetic-field response functions and black-body fluctuations in finite geometries, *Phys. Rev. A* 11 (1) (1975) 230–242.

- [91] J. McMahon, S. Gray, G. Schatz, Nonlocal optical response of metal nanostructures with arbitrary shape, *Phys. Rev. Lett.* 103 (9) (2009) 097403.
- [92] C.C. Williams, H.K. Wickramasinghe, Scanning thermal profiler, *Appl. Phys. Lett.* 49 (23) (1986) 1587.
- [93] U.F. Wischnath, J. Welker, M. Munzel, A. Kittel, The near-field scanning thermal microscope, *Rev. Sci. Instrum.* 79 (7) (2008) 073708.
- [94] S.-A. Biehs, O. Huth, F. Rütting, Near-field radiative heat transfer for structured surfaces, *Phys. Rev. B* 78 (8) (2008) 085414.
- [95] G. Bimonte, Scattering approach to Casimir forces and radiative heat transfer for nanostructured surfaces out of thermal equilibrium, *Phys. Rev. A* 80 (4) (2009) 042102.
- [96] M. Krüger, T. Emig, M. Kardar, Nonequilibrium electromagnetic fluctuations: heat transfer and interactions, *Phys. Rev. Letters* 106 (21) (2011) 210404.
- [97] M. Krüger, G. Bimonte, T. Emig, M. Kardar, Trace formulas for nonequilibrium Casimir interactions, heat radiation, and heat transfer for arbitrary objects, *Phys. Rev. B* 86 (11) (2012) 115423.
- [98] G.A. Domoto, R.F. Boehm, C.L. Tien, Experimental investigation of radiative transfer between metallic surfaces at cryogenic temperatures, *J. Heat Transfer* 92 (3) (1970) 412.
- [99] A. Kittel, W. Müller-Hirsch, J. Parisi, S.-A. Biehs, D. Reddig, M. Holthaus, Near-field heat transfer in a scanning thermal microscope, *Phys. Rev. Lett.* 95 (22) (2005) 224301.
- [100] A. Narayanaswamy, G. Chen, Thermal near-field radiative transfer between two spheres, *Phys. Rev. B* 77 (7) (2008) 075125.
- [101] E.A. Hawes, J.T. Hastings, C. Crofcheck, M.P. Mengüç, Spatially selective melting and evaporation of nanosized gold particles, *Opt. Lett.* 33 (12) (2008) 1383–1385.
- [102] B. Lee, Y.-B. Chen, Z. Zhang, Confinement of infrared radiation to nanometer scales through metallic slit arrays, *J. Quant. Spectrosc. Radiat. Transfer* 109 (4) (2008) 608–619.
- [103] U.F. Wischnath, J. Welker, M. Munzel, A. Kittel, The near-field scanning thermal microscope, *Rev. Sci. Instrum.* 79 (7) (2008) 073708.
- [104] K. Kim, W. Jeong, W. Lee, P. Reddy, Ultra-high vacuum scanning thermal microscopy for nanometer resolution quantitative thermometry, *ACS Nano* 6 (5) (2012) 4248–4257.
- [105] O. Ilic, M. Jablan, J.D. Joannopoulos, I. Celanovic, M. Soljacic, Overcoming the black body limit in plasmonic and graphene near-field thermophotovoltaic systems, *Opt. Express* 20 (10) (2012) A366–84.
- [106] S. Biehs, M. Tschikin, P. Ben-Abdallah, Hyperbolic metamaterials as an analog of a blackbody in the near field, *Phys. Rev. Lett.* 109 (10) (2012) 104301.
- [107] B. Guha, C. Otey, C.B. Poitras, S. Fan, M. Lipson, Near-field radiative cooling of nanostructures, *Nano Lett.* 12 (9) (2012) 4546–4550.
- [108] Y. Guo, C.L. Cortes, S. Molesky, Z. Jacob, Broadband super-Planckian thermal emission from hyperbolic metamaterials, *Appl. Phys. Lett.* 101 (13) (2012) 131106.
- [109] Y. Guo, Z. Jacob, Thermal hyperbolic metamaterials, *Opt. Express* 21 (12) (2013) 15014.
- [110] D.R. Smith, P. Kolinko, D. Schurig, Negative refraction in indefinite media, *J. Opt. Soc. Am. B* 21 (5) (2004) 1032.
- [111] Z. Jacob, I. Smolyaninov, E. Narimanov, Broadband purcell effect: radiative decay engineering with metamaterials, *Appl. Phys. Lett.* 100 (18) (2012). 181105–181105.
- [112] Z. Jacob, J.-Y. Kim, G.V. Naik, A. Boltasseva, E.E. Narimanov, V.M. Shalaev, Engineering photonic density of states using metamaterials, *Appl. Phys. B* 100 (1) (2010) 215–218.
- [113] J.B. Pendry, S.A. Ramakrishna, Near-field lenses in two dimensions, *J. Phys. Condens. Matter* 14 (36) (2002) 8463–8479.
- [114] G.L. Klimchitskaya, V.M. Mostepanenko, The Casimir force between real materials: experiment and theory, *Rev. Mod. Phys.* 81 (4) (2009) 1827–1885.
- [115] A.W. Rodriguez, F. Capasso, S.G. Johnson, The Casimir effect in microstructured geometries, *Nat. Photon.* 5 (4) (2011) 211–221.
- [116] F. London, Zur Theorie und Systematik der Molekularkräfte, *Z. Phys.* 63 (1930) 245.
- [117] S.K. Lamoreaux, Casimir forces: still surprising after 60 years, *Phys. Today* 60 (2) (2007) 40.
- [118] A.J. Hallock, P.L. Redmond, L.E. Brus, Optical forces between metallic particles, *Proc. Natl. Acad. Sci. U.S.A.* 102 (5) (2005) 1280–1284.
- [119] M. Bordag, U. Mohideen, V. Mostepanenko, New developments in the Casimir effect, *Phys. Rep.* 353 (2001) 1–205.
- [120] S.K. Lamoreaux, Demonstration of the Casimir force in the 0.6 to 6 μm range, *Phys. Rev. Lett.* 78 (1) (1997) 5–8.
- [121] U. Mohideen, A. Roy, Precision measurement of the Casimir force from 0.1 to 0.9 μm , *Phys. Rev. Lett.* 81 (21) (1998) 4549–4552.
- [122] A. Roy, U. Mohideen, Demonstration of the nontrivial boundary dependence of the Casimir force, *Phys. Rev. Lett.* 82 (22) (1999) 4380–4383.
- [123] B.W. Harris, F. Chen, U. Mohideen, Precision measurement of the Casimir force using gold surfaces, *Phys. Rev. A* 62 (5) (2000) 052109.
- [124] T. Ederth, Template-stripped gold surfaces with 0.4-nm rms roughness suitable for force measurements: application to the Casimir force in the 20–100-nm range, *Phys. Rev. A* 62 (6) (2000).
- [125] H.B. Chan, V.A. Aksyuk, R.N. Kleiman, D.J. Bishop, F. Capasso, Quantum mechanical actuation of microelectromechanical systems by the Casimir force, *Science (New York, N.Y.)* 291 (5510) (2001) 1941–1944.
- [126] G. Bressi, G. Carugno, R. Onofrio, G. Ruoso, Measurement of the Casimir force between parallel metallic surfaces, *Phys. Rev. Lett.* 88 (4) (2002) 041804.
- [127] T. Emig, A. Hanke, R. Golestanian, M. Kardar, Probing the strong boundary shape dependence of the Casimir force, *Phys. Rev. Lett.* 87 (26) (2001) 260402.
- [128] H. Gies, K. Klingmüller, Casimir effect for curved geometries: proximity-force-approximation validity limits, *Phys. Rev. Lett.* 96 (22) (2006) 220401.
- [129] A. Rodriguez, M. Ibanescu, D. Iannuzzi, F. Capasso, J. Joannopoulos, S. Johnson, Computation and visualization of Casimir forces in arbitrary geometries: nonmonotonic lateral-wall forces and the failure of proximity-force approximations, *Phys. Rev. Lett.* 99 (8) (2007) 080401.

- [130] T. Emig, Casimir-force-driven ratchets, *Phys. Rev. Lett.* 98 (16) (2007) 160801.
- [131] A. Rodriguez, J. Joannopoulos, S. Johnson, Repulsive and attractive Casimir forces in a glide-symmetric geometry, *Phys. Rev. A* 77 (6) (2008) 062107.
- [132] M. Levin, A.P. McCauley, A.W. Rodriguez, M.T.H. Reid, S.G. Johnson, Casimir repulsion between metallic objects in vacuum, *Phys. Rev. Lett.* 105 (9) (2010) 090403.
- [133] J. Bocki, J. Randrup, W. Świątecki, C. Tsang, Proximity forces, *Ann. Phys.* 105 (2) (1977) 427–462.
- [134] O. Kenneth, I. Klich, A. Mann, M. Revzen, Repulsive Casimir forces, *Phys. Rev. Lett.* 89 (3) (2002) 033001.
- [135] F.S.S. Rosa, On the possibility of Casimir repulsion using Metamaterials, *J. Phys. Conf. Ser.* 161 (2009) 12039.
- [136] M. Reid, A. Rodriguez, J. White, S. Johnson, Efficient computation of Casimir interactions between arbitrary 3D objects, *Phys. Rev. Lett.* 103 (4) (2009) 040401.
- [137] K. Pan, A.P. McCauley, A.W. Rodriguez, M.T.H. Reid, J.K. White, S.G. Johnson, Calculation of nonzero-temperature Casimir forces in the time domain, *Phys. Rev. A* 83 (4) (2011) 040503.
- [138] V. Svetovoy, Evanescent character of the repulsive thermal Casimir force, *Phys. Rev. A* 76 (6) (2007) 062102.
- [139] F. Intravaia, C. Henkel, Casimir interaction from magnetically coupled Eddy currents, *Phys. Rev. Lett.* 103 (13) (2009) 130405.
- [140] A.P. McCauley, R. Zhao, M.T.H. Reid, A.W. Rodriguez, J. Zhou, F.S.S. Rosa, J.D. Joannopoulos, D.A.R. Dalvit, C.M. Soukoulis, S.G. Johnson, Microstructure effects for Casimir forces in chiral metamaterials, *Phys. Rev. B* 82 (16) (2010) 165108.
- [141] C. Henkel, K. Joulain, J.-P. Mulet, J.-J. Greffet, Coupled surface polaritons and the Casimir force, *Phys. Rev. A* 69 (2) (2004) 023808.
- [142] F. Intravaia, C. Henkel, A. Lambrecht, Role of surface plasmons in the Casimir effect, *Phys. Rev. A* 76 (3) (2007) 033820.
- [143] A. Lambrecht, I. Pirozhenko, Casimir force between dissimilar mirrors and the role of the surface plasmons, *Phys. Rev. A* 78 (6) (2008) 062102.
- [144] F. Intravaia, A. Lambrecht, Surface plasmon modes and the Casimir energy, *Phys. Rev. Lett.* 94 (11) (2005) 110404.
- [145] V. Hushwater, Repulsive Casimir force as a result of vacuum radiation pressure, *Am. J. Phys.* 65 (5) (1997) 381.
- [146] G.L. Klimchitskaya, U. Mohideen, V.M. Mostepanenko, Pulsating Casimir force, *J. Phys. A: Math. Theor.* 40 (34) (2007) F841–F847.
- [147] I.E. Dzyaloshinskii, E.M. Lifshitz, L.P. Pitaevskii, General theory of van der Waals Forces, *Sov. Phys. Uspekhi* 4 (2) (1961) 153–176.
- [148] J.N. Munday, F. Capasso, V.A. Parsegian, Measured long-range repulsive Casimir–Lifshitz forces, *Nature* 457 (7226) (2009) 170–173.
- [149] R. Decca, D. López, E. Fischbach, D. Krause, Measurement of the Casimir force between dissimilar metals, *Phys. Rev. Lett.* 91 (5) (2003) 050402.
- [150] V.B. Bezerra, G.L. Klimchitskaya, U. Mohideen, V.M. Mostepanenko, C. Romero, Impact of surface imperfections on the Casimir force for lenses of centimeter-size curvature radii, *Phys. Rev. B* 83 (7) (2011) 075417.
- [151] M. Bostrom, B. Sernelius, Thermal effects on the casimir force in the 0.1– 5 μm range, *Phys. Rev. Lett.* 84 (20) (2000) 4757–4760.
- [152] W. Kim, A. Sushkov, D. Dalvit, S. Lamoreaux, Measurement of the short-range attractive force between Ge plates using a torsion balance, *Phys. Rev. Lett.* 103 (6) (2009) 060401.
- [153] H. Failache, S. Saliel, M. Fichet, D. Bloch, M. Ducloy, Resonant van der Waals repulsion between excited Cs atoms and sapphire surface, *Phys. Rev. Lett.* 83 (26) (1999) 5467–5470.
- [154] F. Chen, G.L. Klimchitskaya, V.M. Mostepanenko, U. Mohideen, Demonstration of optically modulated dispersion forces, *Opt. Express* 15 (8) (2007) 4823–4829.
- [155] F. Chen, G.L. Klimchitskaya, V.M. Mostepanenko, U. Mohideen, Control of the Casimir force by the modification of dielectric properties with light, *Phys. Rev. B* 76 (3) (2007) 035338.
- [156] C. Henkel, K. Joulain, J.-p. Mulet, J.-j. Greffet, Radiation forces on small particles in thermal near fields, *J. Opt. A: Pure Appl. Opt.* 4 (5) (2002) S109–S114.
- [157] J. Mehra, Temperature correction to the Casimir effect, *Physica* 37 (1) (1967) 145–152.
- [158] M. Antezza, L. Pitaevskii, S. Stringari, V. Svetovoy, Casimir–Lifshitz force out of thermal equilibrium and asymptotic nonadditivity, *Phys. Rev. Lett.* 97 (22) (2006) 223203.
- [159] A.O. Sushkov, W.J. Kim, D.A.R. Dalvit, S.K. Lamoreaux, Observation of the thermal Casimir force, *Nat. Phys.* 7 (3) (2011) 230–233.
- [160] M. Bordag, B. Geyer, G.L. Klimchitskaya, V.M. Mostepanenko, Casimir force at both nonzero temperature and finite conductivity, *Phys. Rev. Lett.* 85 (3) (2000) 503–506.
- [161] L. Pitaevskii, Thermal Lifshitz force between an atom and a conductor with a small density of carriers, *Phys. Rev. Lett.* 101 (16) (2008) 163202.
- [162] A. Canaguier-Durand, P.A.M. Neto, A. Lambrecht, S. Reynaud, Thermal Casimir effect in the plane–sphere geometry, *Phys. Rev. Lett.* 104 (4) (2010) 040403.
- [163] A.W. Rodriguez, D. Woolf, A.P. McCauley, F. Capasso, J.D. Joannopoulos, S.G. Johnson, Achieving a strongly temperature-dependent Casimir effect, *Phys. Rev. Lett.* 105 (6) (2010) 060401.
- [164] M. Antezza, L. Pitaevskii, S. Stringari, New asymptotic behavior of the surface–atom force out of thermal equilibrium, *Phys. Rev. Lett.* 95 (11) (2005) 113202.
- [165] S. Buhmann, S. Scheel, Thermal Casimir versus Casimir–Polder forces: equilibrium and nonequilibrium forces, *Phys. Rev. Lett.* 100 (25) (2008) 253201.
- [166] C. Noguez, C.E. Román-Velázquez, R. Esquivel-Sirvent, C. Villarreal, High-multipolar effects on the Casimir force: the non-retarded limit, *Europhys. Lett.* 67 (2) (2004) 191–197.
- [167] J. Obrecht, R. Wild, M. Antezza, L. Pitaevskii, S. Stringari, E. Cornell, Measurement of the temperature dependence of the Casimir–Polder force, *Phys. Rev. Lett.* 98 (6) (2007) 63201.
- [168] A.O. Sushkov, W.J. Kim, D.A.R. Dalvit, S.K. Lamoreaux, New experimental limits on non-Newtonian forces in the micrometer range, *Phys. Rev. Lett.* 107 (17) (2011) 171101.